

PAPER • OPEN ACCESS

Weak emergence in the angular dependence of the critical current density of the high temperature superconductor coated conductor REBCO

To cite this article: Paul Branch *et al* 2020 *Supercond. Sci. Technol.* **33** 104006

View the [article online](#) for updates and enhancements.



IOP | ebooks™

Bringing together innovative digital publishing with leading authors from the global scientific community.

Start exploring the collection—download the first chapter of every title for free.

Weak emergence in the angular dependence of the critical current density of the high temperature superconductor coated conductor REBCO

Paul Branch¹, Kozo Osamura²  and Damian Hampshire¹ 

¹ University of Durham, Superconductivity Group, Department of Physics, Durham DH1 3LE, United Kingdom

² Research Institute of Applied Sciences, Kyoto 6068202, Japan

E-mail: Paul.Branch@newcastle.ac.uk

Received 23 March 2020, revised 7 July 2020

Accepted for publication 12 August 2020

Published 3 September 2020



CrossMark

Abstract

Extensive critical current density J_c measurements are reported as a function of magnetic field B , temperature T , angle θ between the applied field and the surface of the tape, and strain ε , on a REBCO coated conductor. The strain, $\varepsilon_{\text{peak}}(B, T, \theta)$, at which $J_c(\varepsilon_{\text{app}})$ is maximised, is a function of B , T , and θ , which is consistent with weakly emergent behaviour. It is described by the chain model that considers competition between twinned domains with different crystallographic orientations and opposing responses under an applied uniaxial strain.

Detailed effective upper critical field $B_{c2}^*(T, \varepsilon_{\text{app}}, \theta = 0)$ data are presented that show universal temperature and strain scaling. They lead to an accurate flux pinning relation for the volume pinning force, $F_p \propto F_{p,\text{max}} b^p (1 - b)^q$, where $b = B/B_{c2}^*(T, \varepsilon_{\text{app}}, \theta = 0)$ and p and q are constants, and are used to help parameterise the scaling behaviour of the angular J_c data more accurately in those cases where B_{c2}^* cannot be measured directly. We derive approximate analytic in-field expressions that explain how the fraction, f , of a -domains amongst the a - and b -domains affects the strain dependence of the critical parameters and conclude that in our tape, $f = 0.4$, and the strain at which J_c is the same in both domains is $\varepsilon_{J_{cA}=J_{cB}} = 0.15\%$. We report a sharp peak in J_c as the applied field approaches alignment with the ab -plane and the unusual result that with it, a suppression of the index of transition N also occurs. We find that the effective upper critical field B_{c2}^* increases as the field angle approaches the ab -plane significantly faster than any available theoretical model for the upper critical field B_{c2} .

In addition, we conclude that a weak-emergence description is not limited to high temperature superconductors, but also describes some low-temperature superconductors.

Keywords: Pinning, critical current density, high magnetic fields

(Some figures may appear in colour only in the online journal)

1. Introduction

High field superconducting magnets are used in a number of state-of-the-art technologies such as magnetic resonance imaging [1,2], fusion [3–6] and high field research magnets



Original content from this work may be used under the terms of the [Creative Commons Attribution 4.0 licence](https://creativecommons.org/licenses/by/4.0/). Any further distribution of this work must maintain attribution to the author(s) and the title of the work, journal citation and DOI.

[7, 8]. In these and other applications there are large gains to be made by being able to achieve higher fields. The present generation of these technologies use low temperature superconductors (LTS), such as Nb-Ti, Nb₃Sn and Nb₃Al. These materials are limited by their relatively low upper critical fields, B_{c2} . In contrast, high temperature superconductors (HTS), such as (RE) Ba₂Cu₃O_{7- δ} (RE = Rare Earth), have the potential to carry far higher currents in high fields due to significantly higher B_{c2} values. This makes them candidate materials for increasing the maximum achievable field in high field magnet technologies. A significant drop in the critical current through high angle grain boundaries in HTS has hindered their development as usable conductors [9, 10]. However, significant progress has been achieved by producing highly textured REBCO tapes where the c -axis is perpendicular to the tape surface [11].

Extensive measurements on technological LTS conductors have been performed over a wide range of field (B), temperature (T) and applied strain (ε_{app}) parameter space, particularly for the A15 compounds [12–23]. There are fewer studies on REBCO tapes, largely due to the relative immaturity of techniques for measuring highly anisotropic HTS samples. There are many limited studies of the strain dependence of REBCO tapes under tensile strain as a function of temperature and field [24–42]. However, as we show in this paper, it is difficult to interpret the data without knowing how J_c behaves in compression. Studies in self-field that do show results in both tension and compression generally show inverted parabolic dependence of the critical current with strain [43–50]. Fewer in-field data are reported. Some reports find, as we do here, that the inverted parabolic behaviour persists at all fields [51, 52]. Whereas other studies report so-called ‘double peak’ behaviour in low fields, returning to inverted parabolic behaviour at higher fields [53, 54]. These differences in samples are probably caused by variations in the pinning properties and are not the focus of this paper.

In this paper we present detailed critical current density measurements as a function of field, field-angle, temperature, and applied tensile and compressive uniaxial strain ($J_c(B, \theta, T, \varepsilon_{\text{app}})$) for a 4 mm wide REBCO tape (Ref: SCS4050) manufactured by SuperPower [55]. The data complement a recent report of J_c obtained with the magnetic field applied at just one fixed angle, normal to the surface of the tape. We report detailed effective upper critical field data measured resistively as a function of temperature and applied uniaxial strain ($B_{c2}^*(T, \varepsilon_{\text{app}})$). The tape does not contain any artificial pinning centres (APC) [56, 57]. It is twinned along the $\{110\}$ planes. This results in two types of domains such that a fraction, f , of the domains are aligned with the $[100]$ direction along the principle axis of strain (i.e. a-axis domains) and the remaining fraction, $(1 - f)$, of domains have the $[010]$ direction along the principle axis of strain [25]. Data from single crystals of REBCO show the strain dependence of the critical parameters (T_c and B_{c2}) is strongly anisotropic and monotonically increasing with tensile strain along the a-axis and monotonically decreasing with tensile strain along the b-axis [58, 59]. Hence, in a tape, there is a bimodal response from the domains to a uniaxial strain. Here we

describe in detail the consequences of the chain model that provides a straightforward explanation of how the inverted parabolic strain behaviour of the critical current in twinned REBCO tapes arises from this bimodal behaviour and shows that the model describes the angular J_c data presented here [50]. This chain model provides quite a different explanation to the standard description for LTS where the peak in the strain dependence of the critical current is attributed to a peak in the intrinsic strain dependence of the critical temperature (T_c) and $B_{c2}(T, \varepsilon_{\text{app}})$ and all the grains show the same dependence (i.e. homogeneous behaviour). The paper also includes a brief analysis of published data for an internal tin Nb₃Sn wire and a Nb₃Al jelly roll wire that demonstrates the chain model description used here for HTS can also describe low temperature superconductors (LTS) [18, 60]. We consider the evidence for grains with different strain dependencies (i.e. multimodal behaviour) [61, 62] as well as discussing the role of grain boundaries.

Preliminary measurements of the angular dependence of the critical current were performed on a REBCO sample taken from the same spool as the sample used in this investigation [51] and demonstrate that at $\theta = 0^\circ$ (when the field is aligned normal to the tape surface) the critical parameters are broadly insensitive to the exact angle at which the field is applied. J_c data taken at $\theta = 0^\circ$ have been published previously [63]. Here we present more results on the same piece of REBCO tape including detailed angular J_c measurements as well as measurements of B_{c2}^* . One of the central questions addressed here is whether the chain model can describe the angular dependence of J_c in the REBCO tape.

In the next section, the experimental methods used to measure the REBCO tape are described. Section 3 gives details of the measurements of the critical current and the effective upper critical field. Section 4 provides engineering parameterisations of the critical current density for all samples. Section 5 reviews the magnetic field and temperature flux pinning scaling. Section 6 provides the mathematical description of the bimodal chain model that describe the strain dependent features of REBCO tape in high fields. Section 7 uses the results presented here to identify the characteristic free parameters from the chain model analysis for our REBCO tape. Sections 8 briefly considers applying the chain model analysis to some data published on LTS superconductors in the literature. Finally, we provide the discussion and the conclusions.

2. Experimental equipment and procedure

Durham’s 15 T, liquid helium cooled, 40 mm wet bore, superconducting split-pair horizontal magnet was used to perform transport critical current density, J_c , and resistive upper critical field measurements, B_{c2}^* , on the REBCO tape. Our $J_c(B, T, \varepsilon_{\text{app}}, \theta)$ probe, which has been described in detail elsewhere [64] uses an inverted temperature cup [65, 66], field corrected thermometry [67], and water-filled bubblers to minimise variations in pressure during the high-current measurements. The sample was soldered to the top of a CuBe

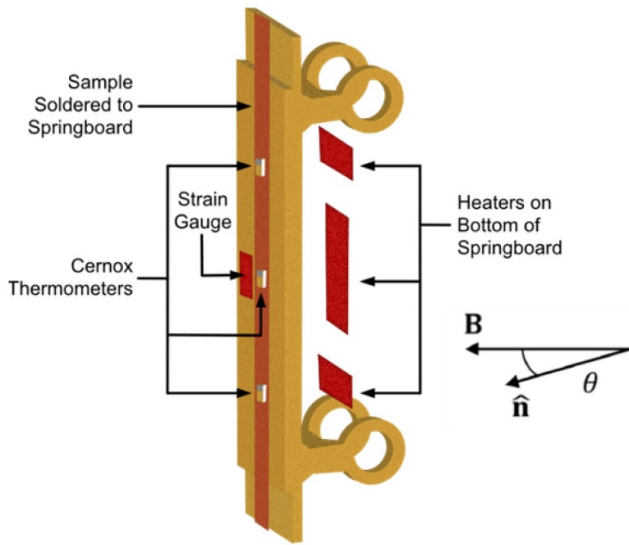


Figure 1. The Springboard sample: The REBCO sample was soldered to the springboard and thermometry, heaters and a strain gauge attached as shown. Either compressive or tensile strain was applied to the sample by pushing the legs of the Springboard together or pulling the legs apart [64].

springboard sample holder using standard 40Sn60Pb solder as shown in figure 1. Since, the soldering temperature for 40Sn60Pb solder is $\sim 240^\circ\text{C}$, which is above the maximum recommended soldering temperature for the tape of 200°C [55], delamination and/or degradation of the sample was a concern. Preliminary experiments at 77 K on samples attached to springboards with either SnPb solder or Bolton 136 (formerly Cerrolow 136) solder (composition 49Bi21In18Sn12Pb, melting point 58°C , soldering temperature $\sim 150^\circ\text{C}$) [68] showed similar strain dependent critical current properties over small strain ranges consistent with the variations expected along the conductor length. This indicated that no delamination or degradation of the tape was caused during the relatively short period of high temperature soldering used for SnPb solder. The SnPb solder was chosen for the main suite of measurements since the Bolton 136 solder was much more susceptible to unpredictable brittle fracture under high strains. In order to reduce helium boil-off, the probe has HTS tapes soldered to the current leads along their length. We have found this makes turning the probe *in-situ* in the split-pair magnet very difficult at high fields probably because of the large magnetisation currents generated by the stray field of the magnet in the HTS current leads. In practice this meant the probe could only be rotated after the applied field had been reduced to below 2 T.

3. Transport measurements

Critical current transport measurements were performed by ramping up the current from 0 A at a constant rate with each measurement taking ~ 60 s. The current and voltage were measured continuously throughout the measurement. We also monitored the strain gauge and found there was no change in strain during the transport measurement. Resistive measurements of the effective upper critical field were made

by applying an excitation current of 100 mA to the sample and increasing the temperature at a rate of 1 Kmin^{-1} while the voltage across the voltage taps and the temperature were monitored continuously. Our intention was to maximise the range of $B - T - \theta$ phase space measured: firstly, dense angular dependent measurements at $\varepsilon_{\text{app}} = 0\%$ and $\varepsilon_{\text{app}} = -1\%$ were made and then in-depth field, temperature and strain dependent measurements were made at selected angles. Relaxation of the experimental probe after thermal cycling between the detailed experimental measurements first made at $\theta = 0$ and the subsequent angular data meant the zero applied strain state for the angular measurements was 0.024% lower than the $\theta = 0$ measurements [63]. All strain values quoted in this paper have been adjusted to account for this.

In these measurements: the angle between the tape and the applied field was determined using a Hall probe mounted on the tape surface; typical noise for the $V - I$ (or equivalently $E - J$) traces measurements was $\sim 30\text{ nV}$; the total current measured differs slightly from the current flowing through the superconducting sample, because some current is shunted through the sample holder and the normal components of the tape. The shunt resistance was determined as a function of field and strain from the resistive measurements of the effective upper critical field. Typical shunt currents were $\sim 80\text{ mA}$ at $100\ \mu\text{Vm}^{-1}$. The shunt correction was applied to all the $V - I$ traces before the critical current was determined at both the $10\ \mu\text{Vm}^{-1}$ and $100\ \mu\text{Vm}^{-1}$ criteria, and the index of transition, N , calculated by fitting the data between $10\ \mu\text{Vm}^{-1}$ and $100\ \mu\text{Vm}^{-1}$ using the definition of N given by $E = E_C \left| (J/J_c)^N \right|$, where E_C is the electric field criterion used to define J_c ; the cross-sectional area of the superconductor was taken to be $4 \times 10^{-3}\ \text{mm}^2$; at the end of all the experiments, the strain was then relaxed to zero and measurements of J_c taken to confirm the reversibility of the sample. These results were found to agree with the data taken at the beginning of the experiments showing the sample remained reversible and undamaged throughout.

Figures 2–7 provide a summary of the important variable-angle transport data. First, dense J_c measurements were taken as a function of θ at $T = 20, 40$ and 60 K , $B = 2$ and 4 T and $\varepsilon_{\text{app}} = 0\%$. Then the strain was taken to $\varepsilon_{\text{app}} = -1\%$ and a second set of dense angular measurements were obtained at the same temperatures and fields. Figure 2 shows these data including, as an inset, the data normalised to the peak value determined by fitting a double Lorentzian at each field and temperature. The peak value of J_c was found to be at $\theta \approx 87.5^\circ$. This is consistent with the *ab*-planes of the REBCO being slightly offset from the plane of the tape [69]. Figure 3 shows these dense angular dependent results when normalised to $J_c(B, T, \varepsilon_{\text{app}} = 0\%, \theta)$. The normalised data are independent of θ and broadly independent of B (particularly at low T). This figure shows that changing the strain changes the absolute value of J_c but broadly does not affect the angular position, shape or normalised size of the angular peaks. Using the dense angular measurements in figure 2, we selected four angles $\theta = 47.5^\circ, 77.5^\circ, 82.5^\circ$ and 87.5° at which in-depth field, temperature and strain dependent J_c measurements

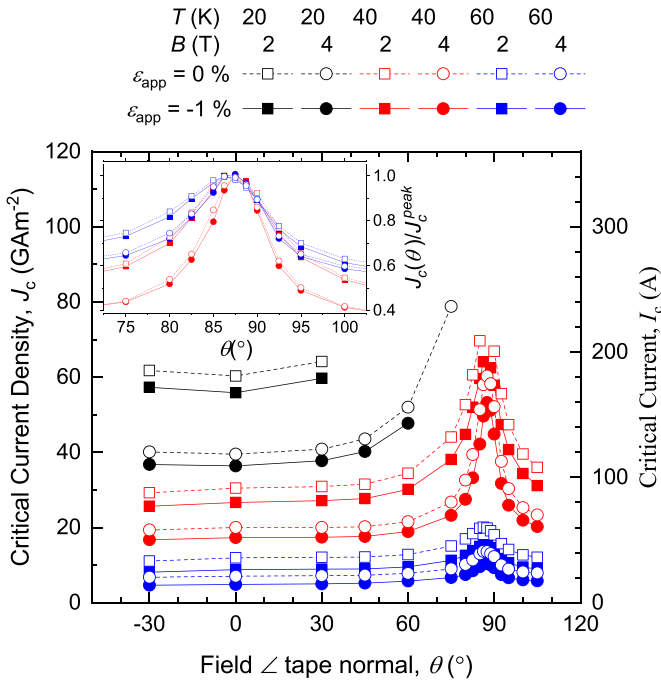


Figure 2. Critical current J_c as a function of angle at applied strains $\varepsilon_{\text{app}} = 0\%$ and -1% and at various magnetic fields and temperatures. Inset: J_c values are normalised to the maximum J_c value that is found by fitting a double Lorentzian to the angular J_c data at and around the peak.

were taken. They were chosen to encompass a large range in J_c values. Starting at $\varepsilon_{\text{app}} = -1\%$, J_c measurements were obtained, at temperatures of 20, 40 and 60 K and fields from 2 to 14 T in intervals of 2 T or until $J_c > 250$ A. The angle was then changed to the next angle and the measurement set repeated until measurements were obtained for all angles. The strain was then increased in intervals of 0.25% to +0.5% and held at each strain where another B , T and θ dependent dataset was obtained. The data obtained are shown in figure 4 and the data at $\theta = 87.5^\circ$ replotted as a function of applied strain in figure 5. As was found at $\theta = 0^\circ$ and is widely observed, the strain dependence of J_c is an inverted parabolic strain behaviour in the region about the peak in the critical current [25, 26, 33, 35, 36, 43, 44, 50, 51, 53, 54] and can be characterised by

$$J_c(\varepsilon_{\text{app}}) = J_c(0) \left(1 + \beta(\varepsilon_{\text{app}} - \varepsilon_{\text{peak}})^2 \right) \quad (1)$$

where ε_{app} is the applied strain, $\varepsilon_{\text{peak}}$ is the applied strain at which the critical current is at its maximum value and β is a constant. We also found $\varepsilon_{\text{peak}}$ is a function of field and temperature dependence as shown in figure 6. The uncertainties in $\varepsilon_{\text{peak}}$ are taken directly from the fitting the data to a parabola given by equation (1). In LTS, the index of transition, N , can be parameterised using the critical current and a modified power law,

$$N = 1 + r_N J_c^{S_N} (B, T, \varepsilon_{\text{app}}) \quad (2)$$

where r_N and S_N are dimensionless constants [20–22, 70, 71]. Figure 7 shows the dense angular dependent results for the

index of transition N as a function of B and T at $\varepsilon_{\text{app}} = 0\%$ and $\varepsilon_{\text{app}} = -1\%$ from which it can be seen that the N -values decrease at angles when the applied field approaches lying along the ab -plane. These results are different to LTS materials where increasing J_c is usually correlated with increasing N -values. We also considered if small uncertainties $\sim 1^\circ$ in the angle caused by not returning the probe to the exact same angle at each applied strain could have caused significant additional uncertainty in the J_c measurements due to the strong angular dependence of J_c . To test this; after the main suite of measurements and reversibility checks, the probe was moved to $\theta = 87.5^\circ$, the strain cycle from $\varepsilon_{\text{app}} = -1\%$ to $\varepsilon_{\text{app}} = +0.5\%$ was repeated without changing the angle between measurements at different strains. At each strain J_c measurements were taken at $B = 4, 10$ and 14 T, and $T = 40$ and 60 K. The J_c and N -value results were compared to equivalent results from the main suite of measurements and were found to agree as shown in figure 5. These data confirm that the uncertainty introduced by returning the angle between different strains, during main suite of measurements did not cause significant uncertainty in J_c and did not significantly affect the values obtained for $\varepsilon_{\text{peak}}$. At the higher angles investigated, temperature and angular dependent r_N and S_N values (cf equation (2)) were required to characterise the data. We attribute this complexity to more than one pinning mechanism operating as discussed below.

In our resistive measurements of the effective upper critical field, three different criteria were considered: extrapolated 0% ρ_N ($B_{c2}^{\text{ex},0\%}$), 50% ρ_N ($B_{c2}^{50\%}$) and extrapolated 100% ρ_N ($B_{c2}^{\text{ex},100\%}$), where ρ_N is the normal state resistivity. Higher current increases the signal to noise ratio in the resistive measurements, whereas using a lower current tends to avoid artefacts from flux flow dissipation. We chose an excitation current of 100 mA across the whole measurement range. We discuss below to what degree the effective upper critical field should be considered similar to the thermodynamic upper critical field and the irreversibility field. The temperature and strain dependence of the effective upper critical field have been parameterised using an equation for high temperature superconductors of the form [72]

$$B_{c2}^*(T, \varepsilon_{\text{app}}) = B_{c2}^*(0, \varepsilon_{\text{app}}) \left(1 - \frac{T}{T_c^*(\varepsilon_{\text{app}})} \right)^s \quad (3)$$

where [17]

$$\frac{T_c^*(\varepsilon_{\text{app}})}{T_c^*(0)} = 1 + c_1 \varepsilon_{\text{app}} + c_2 \varepsilon_{\text{app}}^2 + c_3 \varepsilon_{\text{app}}^3 + c_4 \varepsilon_{\text{app}}^4 \quad (4)$$

$$\frac{B_{c2}^*(0, \varepsilon_{\text{app}})}{B_{c2}^*(0, 0)} = 1 + d_1 \varepsilon_{\text{app}} + d_2 \varepsilon_{\text{app}}^2 + d_3 \varepsilon_{\text{app}}^3 + d_4 \varepsilon_{\text{app}}^4 \quad (5)$$

and the c -values, the d -values, s , and the normalisation parameters $T_c^*(0)$ and $B_{c2}^*(0, 0)$ are fitted constants. Parameterisations were completed using only parabolic terms up to c_2 (and d_2) and listed in table 1. In figure 8, we show the strain and temperature dependence of our $B_{c2}^{\text{ex},100\%}$ dataset for the REBCO tape at $\theta = 0$. The high temperature data are replotted in figure 9 as a universal curve of $B_{c2}^{\text{ex},100\%}(T, \varepsilon_{\text{app}}) / B_{c2}^{\text{ex},100\%}(0, \varepsilon_{\text{app}})$

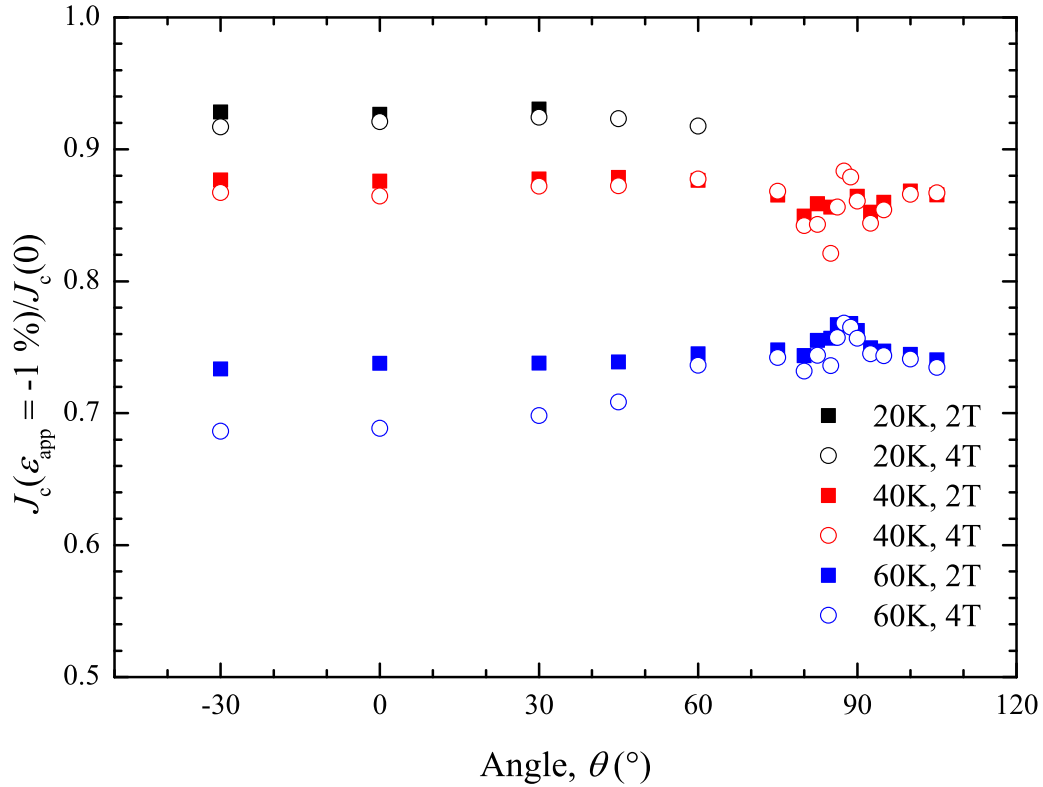


Figure 3. $J_c(\varepsilon_{\text{app}} = -1\%) / J_c(\varepsilon_{\text{app}} = 0\%)$ as a function of angle at different temperatures and fields.

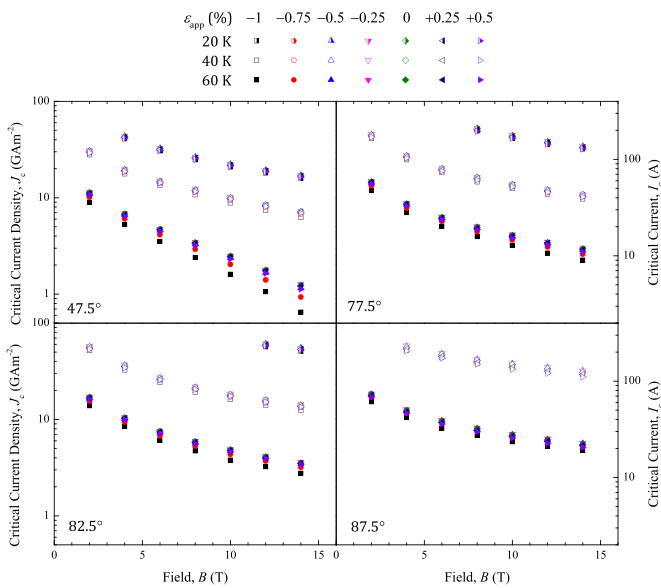


Figure 4. Field, temperature and strain dependence of the critical current density at $\theta = 47.5^\circ, 77.5^\circ, 82.5^\circ$ and 87.5° .

against the reduced temperature, $t = T/T_c^{\text{ex.100\%}}(\varepsilon_{\text{app}})$, demonstrating the accuracy of the universal parameterisation.

4. Engineering parameterisation of $J_c(B, T, \varepsilon_{\text{app}})$

Flux pinning scaling [73–75] is the standard way to describe the in-field critical current of Type II superconductors. Here

Table 1. Parameters of the $B_{c2}^{*\rho}$ parameterisation, eqns (3)–(7) for the REBCO resistive transport data at the three criteria considered in this study where $\theta = 0^\circ$.

	$B_{c2}^{\text{ex.0\%}}$	$B_{c2}^{50\%}$	$B_{c2}^{\text{ex.100\%}}$
RMS Error (mT)	59	44	60
$T_c^{*\rho}(0)$ (K)	88.691	89.056	89.361
c_1 ($10^{-3}\%^{-1}$)	2.187	-0.4492	-2.786
c_2 ($10^{-3}\%^{-2}$)	-16.39	-12.04	-6.580
$B_{c2}^{*\rho}(0,0)$ (T)	86.06	90.49	94.64
d_1 ($10^{-3}\%^{-1}$)	22.34	31.68	36.30
d_2 ($10^{-3}\%^{-2}$)	-103.6	-108.6	-124.7
s	1.309	1.292	1.268

we review the literature for scaling with respect to magnetic field and temperature and then we consider strain.

4.1. Scaling with respect to magnetic field and temperature

When the direction of current flow is perpendicular to the field, the general relation for the flux pinning force density, F_p , is given by

$$F_p = J_c B = C b^p (1 - b)^q \quad (6)$$

where C is a temperature and strain dependent factor, $b = B/B_{c2}^*(T)$ is the reduced field, and p and q are constants. The underlying assumption for eqn (6) is that there is one mode, or one type, of pinning site. This leads to

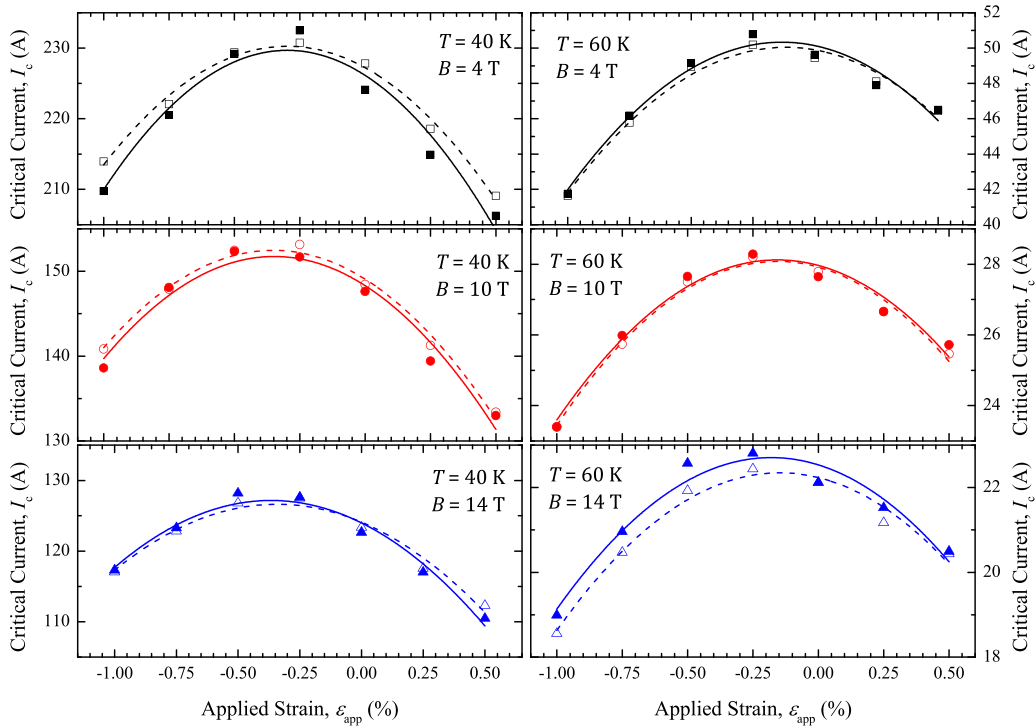


Figure 5. Parabolic fits to the strain dependent critical current data at an angle of $\theta = 87.5^\circ$. Each of the closed symbols (and solid lines) were generated at each strain after the angle between the magnet field and the tape had been cycled. In contrast, the open symbols (and dashed lines) were all generated while the angle between the magnet field and the tape was held fixed.

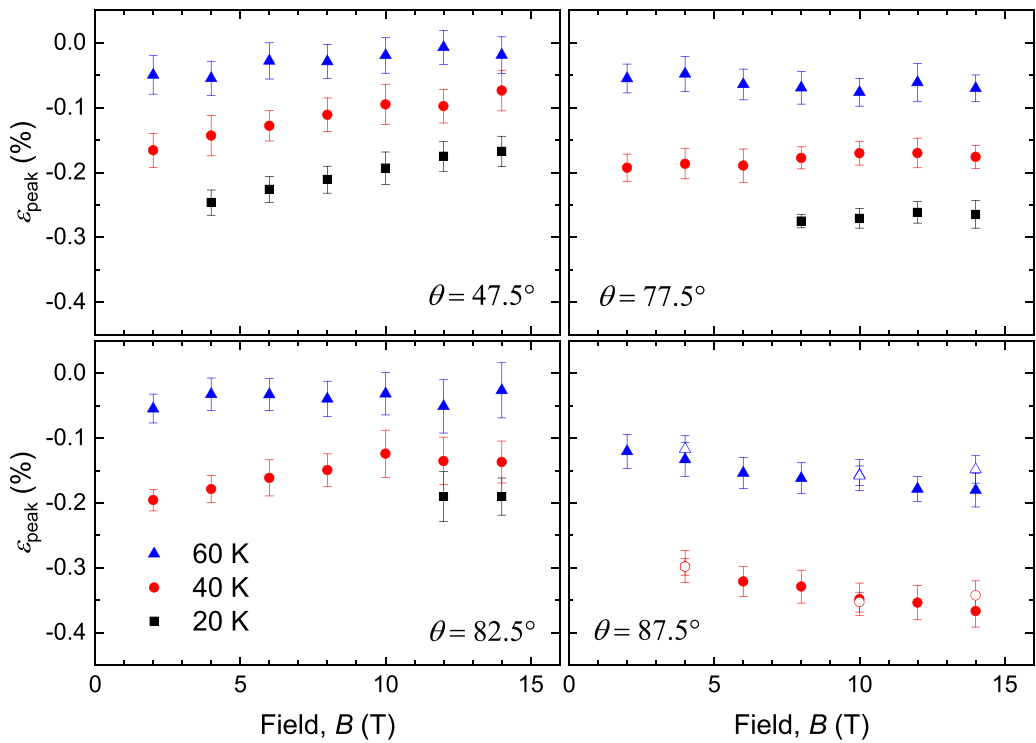


Figure 6. The field and temperature dependence of $\varepsilon_{\text{peak}}$ extracted from parabolic fits to the strain dependent data for (closed symbols) the main data set, where the angle was changed between varying the strain, and (open symbols) the fixed angle data set at $\theta = 87.5^\circ$, where the angle was not changed between varying the strain.

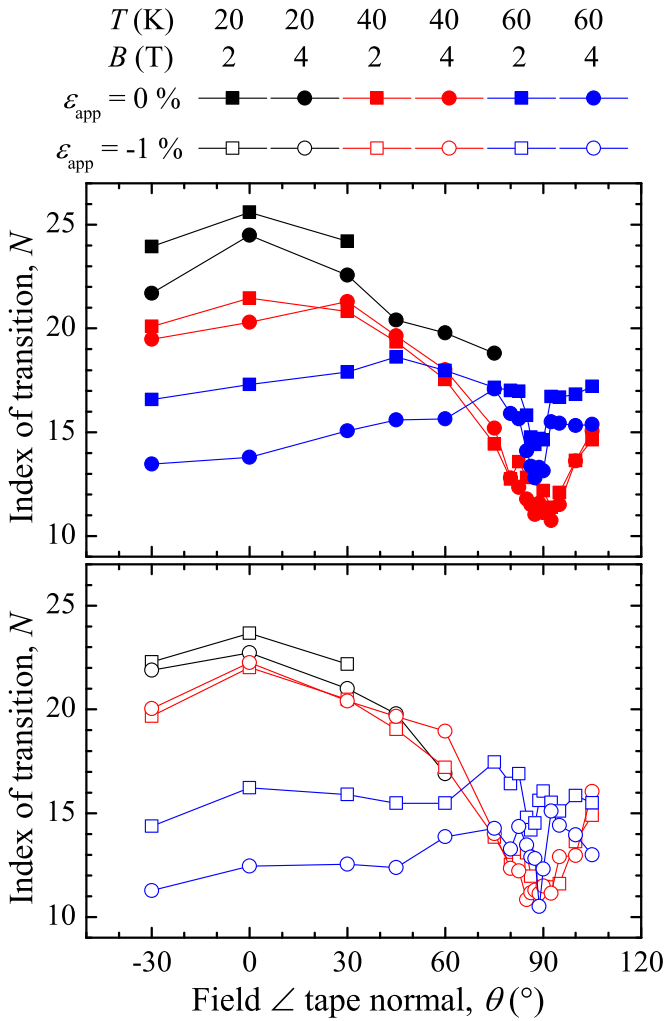


Figure 7. Angular dependence of the N -value at $\varepsilon_{\text{app}} = 0\%$ (upper panel) and -1% (lower panel) at different temperatures and fields.

$$F_p = J_c B = A \frac{[B_{c2}^*]^n}{(2\pi\phi_0)^{1/2} \mu_0 [\kappa_1^*]^m} b^p (1-b)^q \quad (7)$$

where κ_1^* is the Ginzburg-Landau parameter, μ_0 is the vacuum permeability, ϕ_0 is the magnetic flux quantum and n , m , p , q and A are constants and a change in n , p , or q by $1/2$ indicates a change in pinning mechanism [73–75]. It is well known that the correlations between these parameters can be significantly reduced if independent measurements of J_c and B_{c2}^* are made [18]. In early historical flux pinning work, it was assumed that κ_1^* was independent of temperature and a value of n was extracted from the gradient of a $\log F_{p,\text{max}}$ versus $\log B_{c2}^*$ plot [76]. However, more detailed variable temperature data followed on low temperature superconductors, and it was found that the temperature dependence of κ_1^* needed to be included to accurately parameterise the $J_c(B, T, \varepsilon_{\text{app}})$ data [13, 77]. The temperature dependence of κ_1^* is incorporated by taking the Ginzburg-Landau relation for the upper critical field $B_{c2}(T) = \sqrt{2}\kappa_1^*(T)B_c(T)$ [78] along with the two-fluid model for the temperature dependence of the thermodynamic critical field $B_c(T) = B_c(0)(1-t^2)$ [79] where $t = T/T_c^*$ and

the BCS equation for $B_c(0, \varepsilon) = (3\mu_0/2)^{1/2} (3.5/2\pi)\gamma^{1/2}T_c$ [78] where γ is the Sommerfeld constant, to give the equation [18]

$$\kappa_1^* = 924 \frac{B_{c2}^*}{\gamma^{1/2} T_c^* (1-t^2)} \quad (8)$$

Equation (8) implies that the gradient of a $\log(F_{p,\text{max}}[\kappa_1^*]^m)$ versus $\log B_{c2}^*$ gives the value of the exponent n . Computational, experimental and analytic work lead to setting m equal to 2 [17, 75, 77, 80] although different values of the exponent m have also been found useful for more limited datasets [13–16, 81]. We have found that for many Nb₃Sn [17, 19] and Nb₃Al [18] wires, the volume pinning force density is given by equation (7) where $n = 5/2$, $m = 2$, $p = 1/2$, $q = 5/2$ and A is a dimensionless constant $\sim 1/250$ for Nb₃Sn and $\sim 1/100$ for Nb₃Al. When κ_1 is a function of temperature, the value of n can be found by plotting $\log_{10} F_{p,\text{max}}(\kappa_1^*)^2 \cdot \gamma \cdot 924^2$ or equivalently $\log_{10} F_{p,\text{max}}[B_{c2}^*(T)]^2 (T_c^*)^{-2} (1-t^2)^{-2}$ versus $\log_{10} B_{c2}^*$.

4.2. Scaling with respect to strain

Success using magnetic field and temperature scaling, followed by reasonable experimental evidence for universal scaling of F_p with strain, lead to an engineering scaling law that has been successfully used to parameterise the field, temperature and strain dependencies of many low temperature superconducting wires [17, 19–21, 23]

$$J_c(B, T, \varepsilon_{\text{app}}) = A^*(\varepsilon_{\text{app}}) [T_c^*(\varepsilon_{\text{app}})(1-t^2)]^2 \times [B_{c2}^*(T, \varepsilon_{\text{app}})]^{n-3} b^{p-1} (1-b)^q \quad (9)$$

where $A^*(\varepsilon_{\text{app}})$ is a material dependent parameter which is used to improve agreement with experimental results so depends on ε_{app} and may depend on θ , but is independent of B and T . It includes the strain dependence of $\gamma(\varepsilon)$, $T_c^*(\varepsilon_{\text{app}})$, $B_{c2}^*(0, \varepsilon_{\text{app}})$ and $A^*(\varepsilon_{\text{app}})$ that are related by the power laws,

$$\frac{T_c^*(\varepsilon_{\text{app}})}{T_c^*(0)} = \left(\frac{B_{c2}^*(0, \varepsilon_{\text{app}})}{B_{c2}^*(0, 0)} \right)^{\frac{1}{w}} = \left(\frac{A^*(\varepsilon_{\text{app}})}{A(0)} \right)^{\frac{1}{u}} \quad (10)$$

where w and u are constants, and $T_c^*(\varepsilon_{\text{app}})/T_c^*(0)$ is given by the fourth order polynomial in eqn (4). There are in principle 13 free parameters in this parameterisation: $T_c^*(0)$, $B_{c2}^*(0, 0)$, $A(0)$, s , w , u , n , p , q , c_1 , c_2 , c_3 and c_4 . Following the work in [19, 20] w and u were fixed at $w = 2.2$ and $u = 0$. We note that small data sets can be parameterised, with some limited loss of accuracy, using just six free parameters [23]. For the REBCO tape, a reasonably accurate parameterisation, without resistively measured values of B_{c2}^* , was found after splitting the data into two temperature regimes: a) $T \leq 60$ K and b) $T \geq 68$ K where eqn (3) gives the functional form of B_{c2}^* . The free parameters obtained for the $100 \mu\text{Vm}^{-1}$ criterion are given in table 2. We have ensured each fit to the data minimised Chi-squared with Poisson statistics [82]. This approach ensures our fitting parameters remain independent of whether J_c or F_p data were fitted. In the low temperature region the engineering

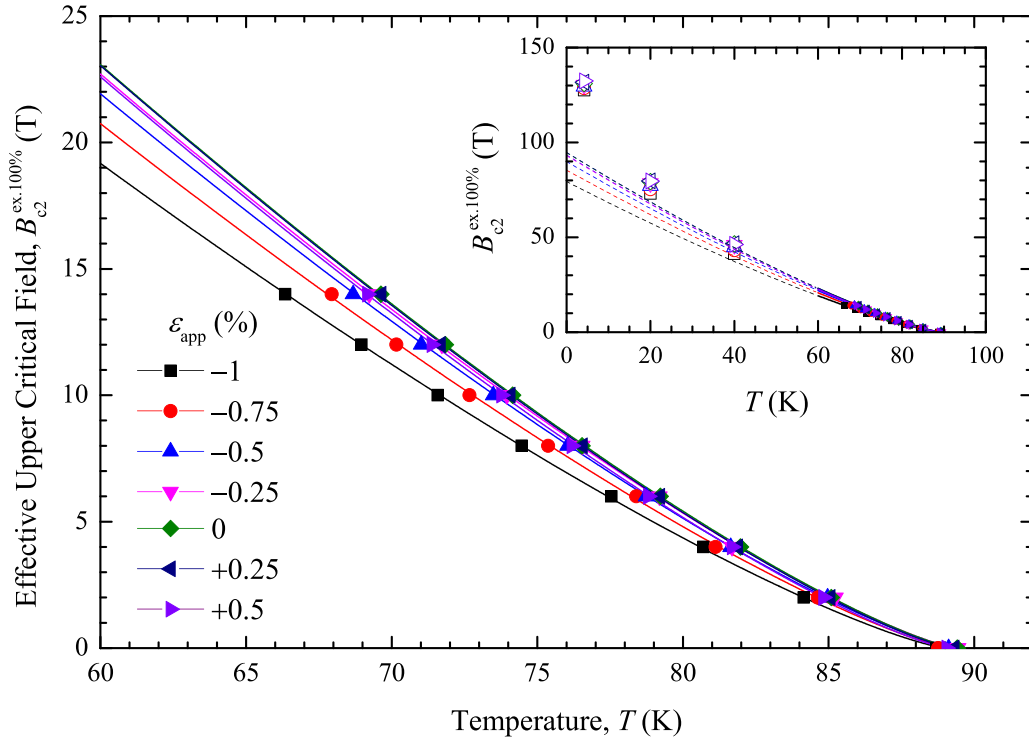


Figure 8. Effective upper critical field of REBCO as a function of temperature and strain for the REBCO tape using the extrapolated 100% criterion. The magnetic field was applied normal to the surface of the tape (i.e. $\theta = 0^\circ$). Closed symbols are from resistance measurements. Open symbols are from extrapolation of the flux pinning scaling curves as detailed in section 5. Solid lines are a parameterisation of the data from resistance measurements using eqn (3) and the dashed lines are the extrapolation of this parameterisation to $T = 0$ K.

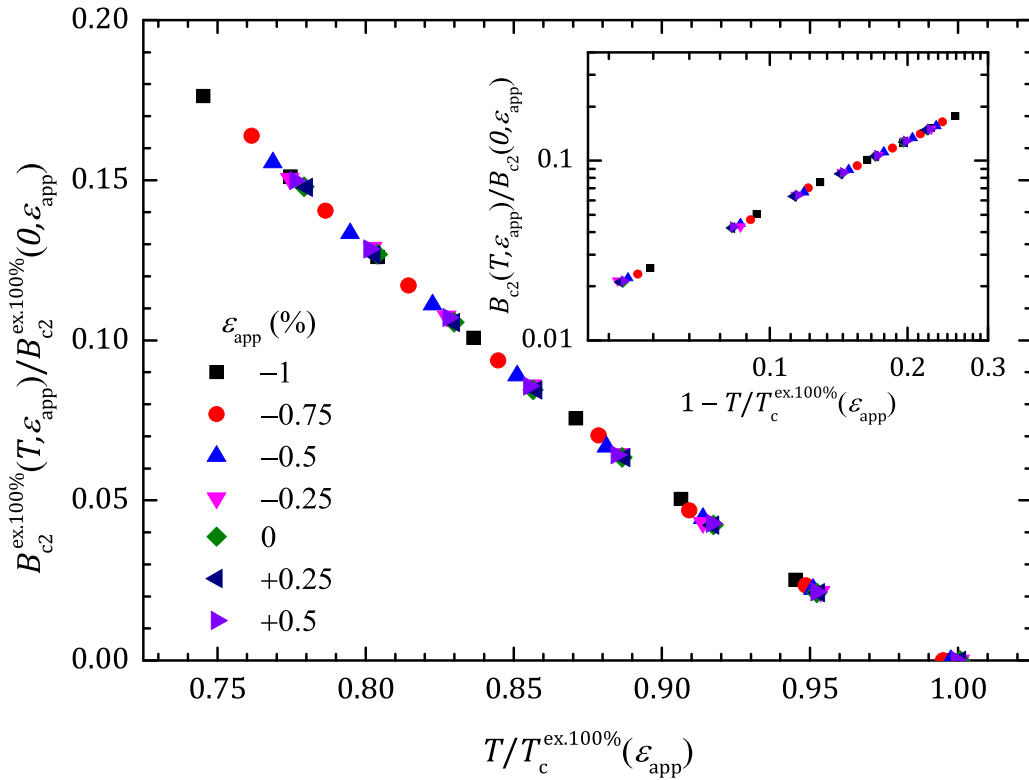


Figure 9. $B_{c2}^{\text{ex.100\%}}(T, \epsilon_{\text{app}}) / B_{c2}^{\text{ex.100\%}}(0, \epsilon_{\text{app}})$ against reduced temperature for the REBCO tape calculated using parameterisation results from eqn (3). The magnetic field was applied normal to the surface of the tape (i.e. $\theta = 0^\circ$). (inset) $B_{c2}^{\text{ex.100\%}}(T, \epsilon_{\text{app}}) / B_{c2}^{\text{ex.100\%}}(0, \epsilon_{\text{app}})$ against one minus the reduced temperature.

scaling law parameterisations includes unphysical constants as has been reported previously [83]. Although such approaches using eqn (9) can provide a useful engineering parameterisation for critical current data, our recent work shows that the effect of magnetic field and temperature on J_c must be treated on a fundamentally different footing to that of strain for an accurate description of the underlying science as shown below [63],

5. $F_p(B, T)$ —Field and Temperature Scaling

5.1 Fixed Angle measurements ($\theta = 0$)

First, we outline our approach to finding the temperature and strain independent p and q values using the data at $\theta = 0$. Eqn (6) is fitted to the data in the region where direct measurements of the resistive upper critical field are available ($T = 60, 68$ and 76 K). $B_{c2}^{*p}(T, \varepsilon_{app})$ is used to calculate the reduced field, b , and $F_{p,max}$ is a free parameter at each temperature and strain. The data were fitted using all combinations of E -field and B_{c2}^{*p} criteria. Four different fitting procedures are used to investigate fully the strain and temperature scaling of the parameters p and q : 1) p and q are independent free parameters at each temperature and strain, 2) p and q are independent free parameters at each temperature only, 3) p is a global parameter and q is an independent free parameter at each temperature, 4) both p and q are single global parameters. Procedures 1 and 2 give similar results: p and q are temperature dependent only and show little strain dependence. The results of fitting procedures 2–4 are summarised in table 3 for all combinations of criteria Procedure 2 shows a relatively strong temperature dependence and can be compared to procedure 3 which makes p a global parameter and q temperature dependent. Procedure 3 has a significant reduction in the temperature dependence for q , which we associate with uncertainties in the determination of p as a result of limited data at low reduced field. The temperature dependence is within the uncertainties of fitting procedure 4, where both p and q are global parameters, for the $B_{c2}^{ex.100\%}$ criterion at both E -field criteria. We conclude that the $B_{c2}^{ex.100\%}$ criterion and J_c values at the $100 \mu Vm^{-1}$ criterion give the most consistent, temperature and strain independent universal scaling in the high temperature region. Hereafter we only report values using these criteria.

Even for $\theta = 0$, direct measurements of $B_{c2}^{ex.100\%}$ are not possible at low temperatures ($T = 4.2, 20, 40$ K) with our 15 T magnet system. In addition, we found extrapolating the parameterisation (cf eqn (3)) did not provide reliable values. Hence, at these temperatures the effective upper critical field, B_{c2}^{*LowT} and $F_{p,max}$ were determined by fitting eqn (6) to the J_c data with p and q fixed at the values obtained for $T \geq 60$ K ($p = 0.56$ and $q = 2.47$). $F_{p,max}$ was taken to be a free parameter at each temperature and strain, and B_{c2}^{*LowT} was characterised as a separate second order function of strain at each temperature given by eqn (6) where the normalisation constant

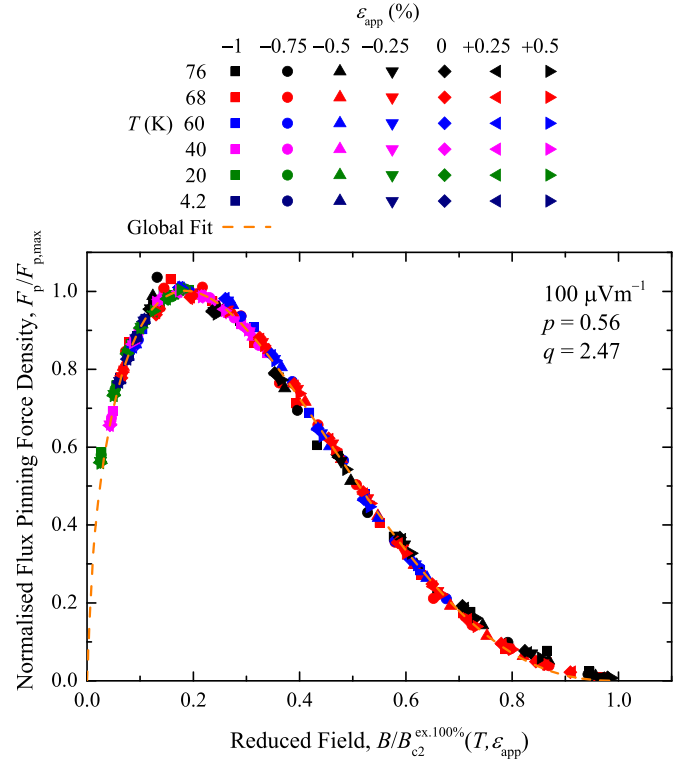


Figure 10. Universal scaling of the volume pinning force, at all temperatures and strains using the $100 \mu Vm^{-1}$ and $B_{c2}^{ex.100\%}$ criteria. The magnetic field was applied normal to the surface of the tape (i.e. $\theta = 0^\circ$). The global fit was determined by the method outlined in Section 5.

is denoted by $B_{c2}^{*LowT}(\varepsilon_{app} = 0\%)$ and $d_3 = d_4 = 0$. The high values of B_{c2}^{*LowT} mean only the initial part of the F_p curve is available at these temperatures, the high gradient of the curve in this region can result in the fitting procedure suggesting a solution with unphysical results where the location of $F_{p,max}$ is clearly incorrect. To account for this the fitting procedure was weighted by $F_p \times B$ so the data near $F_{p,max}$ are preferentially weighted resulting in physically reasonable results. The free parameters obtained from this analysis are summarised in table 4 and are included alongside the direct measurements of B_{c2}^* at high temperatures in the inset of figure 8. The B_{c2}^{*LowT} values are considerably higher than suggested by the parameterisation at high temperature and have a lower strain dependence. Figure 10 shows the universal scaling of the flux pinning curves at $\theta = 0$ for all temperatures and strains. The values of p and q , and the approach to the analysis of data obtained in magnetic fields well below B_{c2}^* , are now applied to our angular data.

5.2. Variable angle Transport Measurements

Figure 3 shows a relatively small field and angular dependence in the ratio $J_c(B, T, \varepsilon, \theta) / J_c(B, T, 0, \theta)$. We use this result to consider how the temperature and strain dependencies of the effective upper critical field B_{c2}^* and the effective

Table 2. Parameters of the engineering parameterisation, eqn (9). The parameters in bold were taken to be fixed [19]. The REBCO data are derived from the $\theta = 0^\circ$ data. The bronze route data were taken from reference [63].

	REBCO 4.2 K $\leq T \leq$ 60 K	REBCO 68 K $\leq T \leq$ 84 K	Nb ₃ Sn Bronze Route	Nb ₃ Sn Internal Tin	Nb ₃ Al Jelly Roll
RMS Error (MAm ⁻²), (A)	600, 2.4	50, 0.20	23, 4.8	11, 2.3	4.9, 1.0
A(0) (MAm ⁻² K ⁻² T ³⁻ⁿ)	0.0625	6.55	45.8	113	66.3
T_c[*](0) (K)	185.0	90.1	16.5	16.6	15.6
B_{c2}[*](0,0) (T)	139.0	98.7	30.7	33.3	26.9
c₁ (% ⁻¹)	0.00224	0.00139	0.107	0.0671	0.0156
c₂ (% ⁻²)	-0.0198	-0.0294	-0.0972	-0.316	-0.0515
c₃ (% ⁻³)	0.00391	0.0104	-0.0806	-0.300	-0.00302
c₄ (% ⁻⁴)	0.00103	0.00520	-0.0291	-0.126	0.00664
w	2.2	2.2	2.2	2.2	2.2
u	0	0	0	0	0
s	5.27	1.26	-	-	-
ν	-	-	1.28	1.35	1.30
n	3.33	2.66	2.44	2.40	2.65
p	0.451	0.581	0.526	0.926	0.702
q	1.44	2.86	1.74	2.82	2.78
r_N	5.59		1.44	1.78	0.775
S_N	0.44		0.50	0.36	0.621

Table 3. Results of fitting the $J_c(B, T, \varepsilon_{app})$ data at $T = 60, 68, 76$ K for REBCO to eqn (6) for all combinations of E -field and B_{c2}^{*p} criteria for $\theta = 0^\circ$. Data are shown for fits performed in three ways: where p and q are independent free parameters at each temperature, where p is a global parameter and q is an independent free parameter at each temperature and where both are p and q global parameters.

T (K)	$B_{c2}^{ex.0\%}$				$B_{c2}^{50\%}$				$B_{c2}^{ex.100\%}$			
	$10 \mu Vm^{-1}$		$100 \mu Vm^{-1}$		$10 \mu Vm^{-1}$		$100 \mu Vm^{-1}$		$10 \mu Vm^{-1}$		$100 \mu Vm^{-1}$	
	p	q	p	q	p	q	p	q	p	q	p	q
60	0.52	2.09	0.51	1.78	0.59	2.56	0.57	2.19	0.64	3.06	0.62	2.63
68	0.37	1.64	0.36	1.35	0.45	2.16	0.44	1.83	0.57	2.89	0.54	2.42
76	0.11	1.17	0.11	0.91	0.24	1.74	0.20	1.34	0.47	2.71	0.36	2.04
60		1.93		1.62		2.38		2.03		2.95		2.50
68	0.43	1.74	0.42	1.44	0.50	2.24	0.49	1.90	0.60	2.94	0.55	2.47
76				1.25		2.10		1.73		2.93		2.37
p and q Global	0.42	1.82	0.40	1.50	0.48	2.28	0.47	1.93	0.59	2.94	0.56	2.47.

critical temperature T_c^* vary as a function of angle. At low temperatures and high angles, in the low reduced field limit $b \ll 1$, Eqn (9) gives the ratio $J_c(B, T, \varepsilon, \theta) / J_c(B, T, 0, \theta)$ to be

$$\frac{J_c(B, T, \varepsilon, \theta)}{J_c(B, T, 0, \theta)} = \frac{A(\theta)}{A(0)} \left[\frac{T_c^*(\varepsilon) \left(1 - \left(\frac{T}{T_c^*(\varepsilon)} \right)^2 \right)}{T_c^*(0) \left(1 - \left(\frac{T}{T_c^*(0)} \right)^2 \right)} \right]^2 \times \left(\frac{B_{c2}^*(T, \varepsilon, \theta)}{B_{c2}^*(T, 0, \theta)} \right)^{n-p-2} \quad (11)$$

We choose to separate the effective upper critical field into a component describing the functional form $f(T, \varepsilon, \theta)$ and a normalisation constant $B_{c2}^*(0, \varepsilon, \theta)$ to give $B_{c2}^*(T, \varepsilon, \theta) =$

$$B_{c2}^*(0, \varepsilon, \theta) f(T, \varepsilon, \theta)$$

$$\frac{J_c(B, T, \varepsilon, \theta)}{J_c(B, T, 0, \theta)} = \left(\frac{T_c^*(\varepsilon)}{T_c^*(0)} \right)^2 \left(\frac{1 - t^2(\varepsilon)}{1 - t^2(0)} \right)^2 \times \left(\frac{B_{c2}^*(0, \varepsilon, \theta) f(T, \varepsilon, \theta)}{B_{c2}^*(0, 0, \theta) f(T, 0, \theta)} \right)^{n-p-2} \quad (12)$$

Using the relation $B_{c2}^*(0, \varepsilon, \theta) / B_{c2}^*(0, 0, \theta) = (T_c^*(\varepsilon) / T_c^*(0))^w$ where w is a constant [19, 20] gives

$$\frac{J_c(B, T, \varepsilon, \theta)}{J_c(B, T, 0, \theta)} = \left(\frac{T_c^*(\varepsilon)}{T_c^*(0)} \right)^2 \left(\frac{1 - t^2(\varepsilon)}{1 - t^2(0)} \right)^2 \times \left(\left(\frac{T_c^*(\varepsilon)}{T_c^*(0)} \right)^w \frac{f(T, \varepsilon, \theta)}{f(T, 0, \theta)} \right)^{n-p-2} \quad (13)$$

Table 4. Results of determining B_{c2}^{*LowT} ($T = 0, \theta = 0$) at $T = 4.2, 20, 40$ K for REBCO tape at the $100 \mu V m^{-1}$ E -field criterion. The flux pinning curve, eqn (6), is fitted to the J_c data with $p = 0.56$ and $q = 2.47$ (the values obtained from the flux pinning analysis at $T = 60, 68, 76$ K). B_{c2}^{*LowT} is a second order function of strain at each temperature, eqn (7) where we set $d_3 = d_4 = 0$.

T (K)	B_{c2}^{*LowT} ($T = 0, \theta = 0$) (T)	d_1 ($10^{-3}\%$)	d_2 ($10^{-3}\%$)
4.2	131	22	-5
20	79	31	-48
40	46.5	31	-80

This equation shows there is no field dependence for the ratio $J_c(B, T, \varepsilon_1, \theta) / J_c(B, T, \varepsilon_2, \theta)$ but there is a temperature dependence. These predictions are in agreement with the experimental data shown in figures 2 and 3 and hence that the parameters w, n, p are independent of angle. The arguments break down at $B = 4$ T, $T = 60$ K and $\theta \neq 90^\circ$, which is attributed to the low reduced field limit not being applicable.

One of the most important features of a flux pinning scaling curve is the location of $F_{p,max}$, which for a universal scaling curve occurs at the same value of b independent of temperature, strain and angle. Most of the angular data are in magnetic fields that are even below that at which $F_{p,max}$ occurs. Because the turning point in F_p at $F_{p,max}$ is only captured at the lowest angle, fitting procedures using standard weighting techniques leads to F_p curves which gave unphysical values of $F_{p,max}$ and B_{c2}^* . The high gradient of the F_p curve at very low reduced field and the small reduced field region over which the data are fitted are responsible for this, making the results of the fitting relatively insensitive to large variations in the effective upper critical field. To lower the impact of this, again the data were weighted by $F_p \times B$ forcing the fitting procedure to weight data closer to $F_{p,max}$ more heavily which resulted in more physically reasonable scaling curves. Figure 11 shows the universal flux pinning scaling curve obtained and the inset shows the values of $B_{c2}^*(T, \varepsilon_{app}, \theta) / B_{c2}^*(T, \varepsilon_{app}, \theta = 0^\circ)$. The inset data do not show a consistent temperature dependence and the error bars are very large. Nevertheless we have tried to fit the B_{c2}^* data using the predicted forms from anisotropic Ginzburg-Landau theory [84–87], Klemm's theory [88, 89] and the extreme theoretical case of the 2D Tinkham model [90] for thin films and found that none of them can describe the very sharp angular dependence for B_{c2}^* .

To find the temperature and strain scaling of B_{c2}^* and $F_{p,max}$, first we consider the $\theta = 0$ data where we have direct measurements of B_{c2}^* . B_{c2}^* is characterised using eqns (3)–(7) for the $B_{c2}^{ex.100\%}$ criterion at $T = 60, 68, 76$ K, and eqns (7) and (6) at $T = 4.2, 20, 40$ K and $F_{p,max}$ is an independent fitted parameter at each temperature and strain. If we simply produce a historical plot of $F_{p,max}$ as a function of B_{c2}^* on a log-log scale. The gradient of the data (cf n in eqn (7)) is a function of both temperature and strain and has values lower than n expected from flux pinning considerations [73, 75]. At low temperatures, where we expect the effects of the variation of T_c , within the material to have little effect, the gradient of the data is nearly a factor of two different when determined by

strain rather than temperature (i.e. 0.84 and 1.74 respectively). Figure 12 shows the results of $F_{p,max}[\kappa_1^*]^2$ vs B_{c2}^* on a log-log plot for the variable angle data including the data at $\theta = 0^\circ$. The solid line is a linear fit to the data, which gives a value of $n = 2.85$ for $m = 2$. The variable angle data follow the same trends as those found at zero angle. This confirms that equation (11) gives a reasonably good approximation for the temperature dependence of κ_1^* . However, n is still not constant and double-valued behaviour of $F_{p,max}$ as a function of B_{c2}^* is still present. Other values of m were investigated and strain dependent values of γ (or equivalently A) were considered [13–16, 18–20, 23, 81] but none were found to be significantly better than $m = 2$.

We note that because the scaling analysis has been completed at each temperature and each strain with no *a priori* assumptions made about the dependence of $F_{p,max}$ on B_{c2}^* , it has enabled the identification of the double valued behaviour of $F_{p,max}[\kappa_1^*]^2$ versus B_{c2}^* and a temperature dependence for the exponent n . These features cannot be identified from using the engineering parameterisation (cf Table 2) because it assumes $F_{p,max}$ is a singled valued function B_{c2}^* . We also note that the engineering parameterisation assumes that ε_{peak} is independent of B and T , which is in contradiction with the detailed experimental data.

6. The bimodal chain model for REBCO

Historically, flux pinning scaling laws, used to describe LTS materials, assumed the superconducting material was broadly homogenous so all the grains respond the same manner and the critical parameters, T_c^* , B_{c2}^* and J_c have a similar response to uniaxial strain. The community anchored J_c versus strain data at a particular peak value, ε_{peak} , that was the applied strain at which all the critical parameters including $J_c(\varepsilon_{app})$ was at its optimum. More recently [63], the authors have shown that ε_{peak} is a function of magnetic field and temperature consistent with twinning in the REBCO tape that results in some [91] domains aligned with the direction of applied strain (domain A) and other domains with [010] aligned with the direction of applied strain (domain B). In practice when applying strain, in some domains the critical parameters increase, whereas in other domains they decrease (i.e. a bimodal material). In this section we first outline the bimodal chain model, developed to describe the strain dependence of REBCO tapes in zero field [50]. It is a one-dimensional model in which strain is applied along the axis of the tape. Then we outline the extension of the model to consider the role of magnetic field and temperature [63]. This enables us to determine whether the simple chain model can describe the angular J_c data presented here for the REBCO tape.

In order to avoid any confusion with the well-established definition of intrinsic strain (i.e. $\varepsilon_{int} = \varepsilon_{app} - \varepsilon_{peak}$) two new characteristic strains are defined: the domain strain, ε_{JD} , where

$$\varepsilon_{JD} = \varepsilon_{app} - \varepsilon_{JcA=JcB} \quad (14)$$

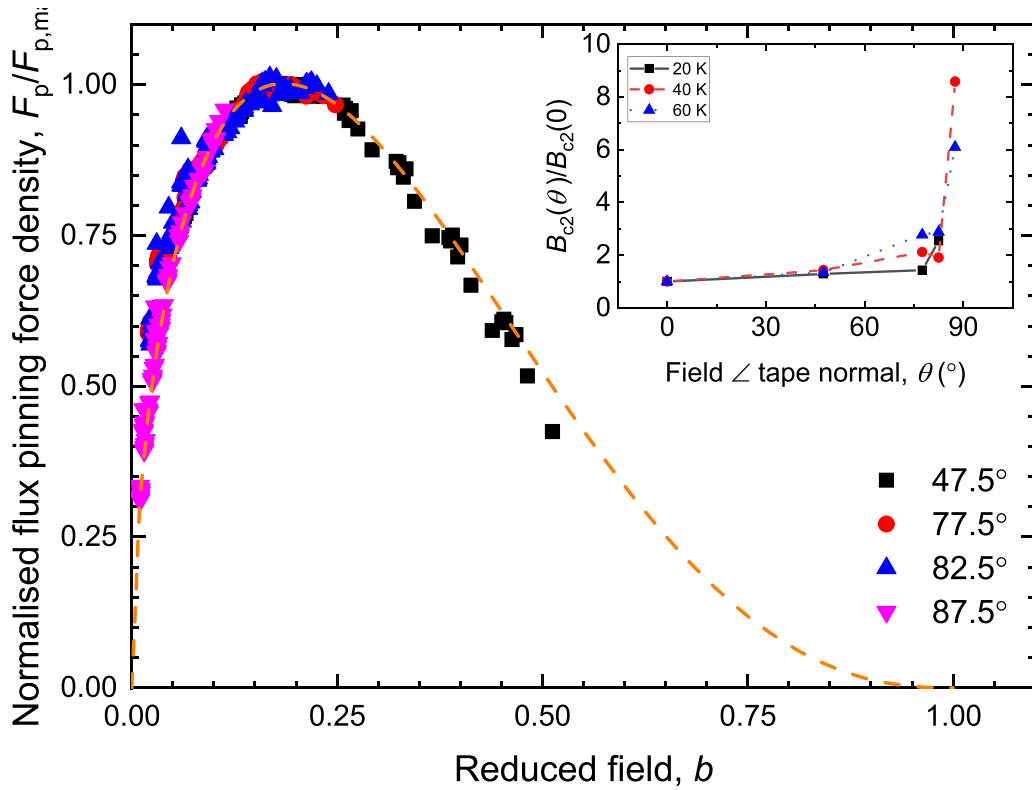


Figure 11. Normalised flux pinning scaling curve versus reduced field found by fixing the parameters $p = 0.56$ and $q = 2.47$ to their values determined at $\theta = 0^\circ$. $F_{p,max}$ and B_{c2}^* are unconstrained temperature, strain and angular dependent free parameters. Best fits are found by weighting the data by $F_p \times B$. (inset) $B_{c2}(\theta)/B_{c2}(0)$ as a function of angle and temperature.

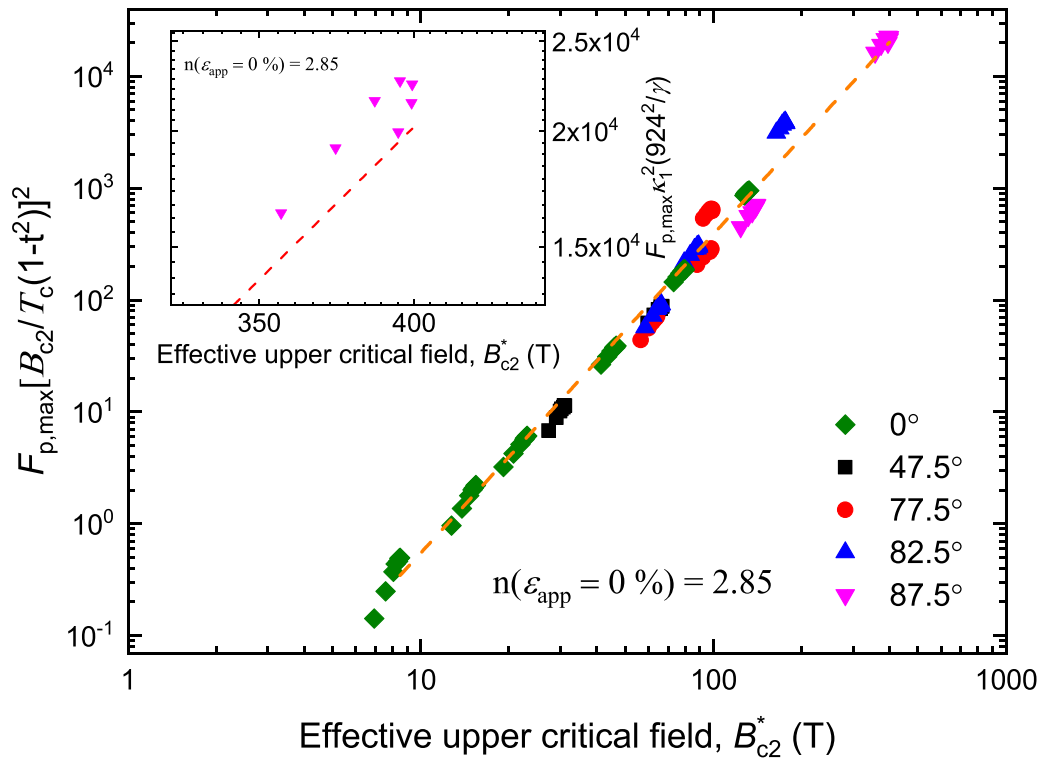


Figure 12. Maximum flux pinning force density multiplied by the square of the Ginzburg–Landau parameter, κ_1^* , against the effective upper critical field on a log-log scale for the REBCO tape at the $100 \mu V m^{-1}$ E -field criterion and extrapolated 100% B_{c2}^* criterion including the data at 0° from the previous study. B_{c2}^* is determined using eqn (3) at $T = 60, 68, 76$ K, and eqns (7) and (6) at $T = 4.2, 20, 40$ K as detailed in Section 5. The dashed line is a linear fit at $\epsilon_{app} = 0\%$ Detail of the data at 40 K showing double valued behaviour of $F_{p,max}$.

and $\varepsilon_{J_{cA}=J_{cB}}$ is the applied strain at which the critical current density in both domains (A and B) are equal or equivalently, ε_{JD} is zero when the critical current density in both domains are equal. The magnitude of $\varepsilon_{J_{cA}=J_{cB}}$ is again broadly determined by the differential thermal contraction produced by the sample holder and the matrix materials and hence, to first order, is constant for any particular experimental set-up because the strain under which $J_{cA} = J_{cB}$ will remain constant because the field and temperature dependence of J_c in both domains is taken to be the same. The second characteristic strain characterises the difference between $\varepsilon_{J_{cA}=J_{cB}}$ and the applied strain at which J_c reaches its maximum, ε_{peak} . By definition

$$\varepsilon_{p,JD} = \varepsilon_{peak} - \varepsilon_{J_{cA}=J_{cB}} \quad (15)$$

where we call $\varepsilon_{p,JD}$ the peak domain strain which (along with ε_{peak}) is field and temperature dependent and $\varepsilon_{J_{cA}=J_{cB}}$ is constant. Eqn (15) does not include the applied strain because it characterises the underlying behaviour of the superconducting material.

6.1. Bimodal chain model for twinned domains in zero field

The bimodal chain model considers two twinned domains, A and B, with domain fractions f and $(1-f)$ respectively [50]. To simplify the mathematics, they are connected in series (i.e. in a chain) and following single crystal data, the effective critical temperatures of each domain have opposing strain dependencies,

$$T_{ci}^* = \begin{cases} T_c^*(0) + \left. \frac{dT_{cA}^*}{d\varepsilon_{JD}} \right|_{\varepsilon_{JD}=0\%} \varepsilon_{JD}, & i = A, \\ T_c^*(0) - \left. \frac{dT_{cB}^*}{d\varepsilon_{JD}} \right|_{\varepsilon_{JD}=0\%} \varepsilon_{JD}, & i = B, \end{cases} \quad (16)$$

where $T_c^*(0)$ is the effective critical temperature at $\varepsilon_{JD} = 0\%$. The parameter g_i , is introduced such that at strains close to $\varepsilon_{JD} = 0\%$, the strain dependence of J_{ci} in each domain is linear and opposite,

$$J_{ci}(\varepsilon_{JD}) = \begin{cases} J_c(0)(1 + g_A \varepsilon_{JD}), & i = A, \\ J_c(0)(1 - g_B \varepsilon_{JD}), & i = B, \end{cases} \quad (17)$$

where $g_i = (1/J_c(0)) |\partial J_{ci} / \partial \varepsilon_{JD}|_{\varepsilon_{JD}=0\%}$, J_{ci} is the critical current in domain i and $J_c(0)$ is the critical current at $\varepsilon_{JD} = 0\%$. It is assumed $g_A = g_B = g$ and each domain is assumed to follow the same power law for the index of transition. The E -field generated by the chain is given by

$$E = E_c f \left(\frac{J}{J_{cA}} \right)^{N_A} + E_c (1-f) \left(\frac{J}{J_{cB}} \right)^{N_B} \quad (18)$$

where E_c is the E -field criterion. It is also assumed $N_A = N_B = N$ hence, the critical current of the whole chain, J_{cT} , is given by

$$J_{cT} = J_c(0) \left[f(1 + g\varepsilon_{JD})^{-N} + (1-f)(1 - g\varepsilon_{JD})^{-N} \right]^{-\frac{1}{N}} \quad (19)$$

By taking a second order Taylor series approximation about $\varepsilon_{JD} = 0\%$ the following expression for $\varepsilon_{p,JD}$ was found [50]

$$\varepsilon_{p,JD} = \frac{2f-1}{4f(1-f)} \frac{1}{g(N+1)} \quad (20)$$

When $f = 0.5$, $\varepsilon_{p,JD} = 0\%$, which is field and temperature independent and replicates the result for a homogeneous material. When $f < 0.5$, $\varepsilon_{p,JD} < 0\%$ and when $f > 0.5$, $\varepsilon_{p,JD} > 0\%$.

6.2. Bimodal chain model for twinned domains in high magnetic fields

Now we consider the in-field behaviour in detail [63]. The parameter α_{Jc} is introduced which accounts for different strain sensitivity in the A- and B- directions and is defined by

$$\alpha_{Jc} = \left. \frac{dJ_{cB}^*}{d\varepsilon_{JD}} \right|_{\varepsilon_{JD}=0\%} / \left. \frac{dJ_{cA}^*}{d\varepsilon_{JD}} \right|_{\varepsilon_{JD}=0\%} = g_B/g_A \quad (21)$$

where one can also write down an equivalent definition for α_{Tc} in terms of the derivatives of T_{cA}^* and T_{cB}^* . By setting the condition $E = E_c$ in Eqn. (18), we find,

$$1 = f \left(\frac{J_{cT}}{J_{cA}} \right)^{N_A} + (1-f) \left(\frac{J_{cT}}{J_{cB}} \right)^{N_B} \quad (22)$$

The transcendental nature of J_{cT} shown in eqn (22) rules out simple analytic solutions. Nevertheless, to develop an insight into the field and temperature dependence of ε_{peak} , one can derive approximate analytic expressions for $\varepsilon_{p,JD}$. Using a second order Taylor expansion for J_{cT} about $\varepsilon_{JD} = 0\%$ from Eqn (22), and comparing the coefficients to eqn (1), an analytic expression is found for the peak domain strain, $\varepsilon_{p,JD}$, as a function of f , α_{Jc} and g_A , given by

$$\begin{aligned} \varepsilon_{peak} - \varepsilon_{J_{cA}=J_{cB}} &= - \left(\frac{dJ_{cT}}{d\varepsilon_{JD}} \right)_{\varepsilon_{JD}=0\%} / \left(\frac{d^2 J_{cT}}{d\varepsilon_{JD}^2} \right)_{\varepsilon_{JD}=0\%} \\ &= \frac{f - \alpha_{Jc}(1-f)}{f(1-f)(1 + \alpha_{Jc})^2} \frac{F(N_0, S_N)}{g_A(B, T)} \end{aligned} \quad (23)$$

where the parameter $F(N_0) = N_0 / (N_0(N_0 + 1) - 2S_N(N_0 - 1))$, N_0 is the index of transition at $\varepsilon_{JD} = 0\%$, S_N is defined in eqn (2) and g_A contains the temperature and field dependencies. We note that in the limit where $\alpha = 1$ and $N_0(N_0 + 1) \gg 2S_N(N_0 - 1)$ (cf typical values for S_N and N_0 are 0.4 and 10 respectively), $F(N_0) \approx 1/(N_0 + 1)$ and eqn (23) reduces to eqn (20).

Eqn (24) requires an explicit evaluation of g_A which we calculate as follows: we approximate the strain dependence of J_{ci} in each domain to be linear in the region of $\varepsilon_{JD} = 0\%$, as in eqn (17). Taking the derivative of eqn (9) g_i is given by

$$g_i = \left| \frac{dT_{ci}^*}{d\varepsilon_{JD}} \right|_{\varepsilon_{JD}=0\%} \left[\frac{2}{T_c^*(0)} \frac{1+t^2(0)}{1-t^2(0)} \right] + \left[B_{c2i}^{*-1}(T,0) \frac{d}{d\varepsilon_{JD}} (B_{c2i}^*(T,\varepsilon_{JD})) \right]_{\varepsilon_{JD}=0\%} \left(\frac{qb(0)}{1-b(0)} + n - p - 2 \right) \quad (24)$$

where $t(\varepsilon_{JD}=0\%) = T/T_c^*(0)$ and $b(\varepsilon_{JD}=0\%) = B/B_{c2}^*(T,0)$ are the reduced temperature and field at $\varepsilon_{JD}=0\%$ respectively. If we take the HTS parameterisation of $B_{c2i}^*(T,\varepsilon_{JD})$ (cf eqn (3)), we obtain

$$g_{i,HTS} = \left| \frac{dT_{ci}^*}{d\varepsilon_{JD}} \right|_{\varepsilon_{JD}=0\%} \frac{1}{T_c^*(0)} \left[2 \frac{1+t^2(0)}{1-t^2(0)} \times + \left(\frac{st(0)}{1-t(0)} + w \right) \left(\frac{qb(0)}{1-b(0)} + n - p - 2 \right) \right] \quad (25)$$

Eqn (25) shows that g_i is proportional to $|dT_{ci}^*/d\varepsilon_{JD}|_{\varepsilon_{JD}=0\%}$ which implies that the scaling law leads to $\alpha_{J_c} = \alpha_{T_c} = \alpha$.

In general, the index of transition in each domain, N_i , is field, temperature and strain dependent. It is parameterised as a function of the critical current given by eqn (2). Hence, the $E-J$ relation of the whole chain, eqn (18), no longer strictly obeys the simple power law. However, we can determine an approximate expression for index of transition for the whole chain, N_T , by replacing the left-hand-side of eqn (18) with $E_c(J/J_{cT})^{N_T}$, differentiating w.r.t. J and setting $J = J_{cT}$. This gives

$$N_T \approx f N_A \left(\frac{J_{cT}}{J_{cA}} \right)^{N_A} + (1-f) N_B \left(\frac{J_{cT}}{J_{cB}} \right)^{N_B} \quad (26)$$

from which values of N_T for the chain model can be calculated.

6.3. Numerical results for the bimodal chain model

In this section we present the in-field behaviour of the bimodal chain model through the parameters J_{cT} and N_T . The critical current in each domain, J_{ci} , is defined using the generalised flux pinning scaling relation of the form of eqn (7) where A^* is taken to be a constant, T_c^* and B_{c2}^* are unique to each domain and the strain dependence is constrained by a linear strain dependence for T_{ci} given by eqn (16).

Table 5 provides the free parameter values used: $T_c^*(0)$, $B_{c2}^*(0,0)$, s and S_N are taken as approximations to the experimental parameters, n , p and q are taken as the Kramer values [75], A and r_N are chosen such that N -values are in agreement with experiment, $dT_{cA}^*/d\varepsilon_{JD}|_{\varepsilon_{JD}=0\%}$ is taken to be $2.5 \text{ K}\%^{-1}$ (cf Tables 6 and 7), and w is taken to be 3 [15]. Eqn (22) is solved numerically for J_{cT} . In figures 13–17, we consider the most simple case, $\alpha_{J_c} = \alpha_{T_c} = \alpha = 1$. Figure 13 shows how different domain fractions (i.e. different values of f) affect the field and temperature dependence of $\varepsilon_{p,JD}$ for $\alpha = 1$. We find the strain at which J_{cT} reaches its peak value (i.e. $\varepsilon_{\text{peak}}$) is a function of field and temperature. For $\alpha = 1$: for the special

Table 5. Parameters ‘used in the numerical calculation of the 1D chain model.

Parameter	Value	Parameter	Value
A	10	n	2.5
$T_c^*(0)$	90 K	m	2.0
$B_{c2}^*(0,0)$	100 T	p	0.5
$\left. \frac{dT_{ci}^*}{d\varepsilon_{JD}} \right _{\varepsilon_{JD}=0\%}$	$2.5 \text{ K}\%^{-1}$	q	2
w	3	r_N	90
s	1.25	S_N	0.4

Table 6. Values of the domain fraction, f , determined using various experimental values of $dT_{ci}^*/d\varepsilon$ from literature, along with a speculative result for $\alpha = 1$ and $dT_{cA}^*/d\varepsilon = 1.6 \text{ K}\%^{-1}$. The results of Welp *et al.* [59] and Fietz *et al.* [58] are converted from stress to strain using a Young’s moduli of 162.7 GPa along the a -axis and 178.1 GPa along the b -axis [92].

	$dT_{cA}^*/d\varepsilon \text{ (K}\%^{-1}\text{)}$	$dT_{cB}^*/d\varepsilon \text{ (K}\%^{-1}\text{)}$	α	f
Suzuki <i>et al.</i> [93]	$+4.09 \pm 0.02$	-2.09 ± 0.01	0.51	0.13
Fietz <i>et al.</i> [58]	$+1.6 \pm 0.1$	-2.1 ± 0.1	1.31	0.34
Welp <i>et al.</i> [59]	$+3.3 \pm 0.3$	-3.4 ± 0.4	1.03	0.21
	+1.6	-1.6	1	0.32

case of $f = 0.5$, the bimodal model predicts behaviour similar to homogeneous materials; when $f < 0.5$, $\varepsilon_{p,JD} < 0\%$; when $f > 0.5$, $\varepsilon_{p,JD} > 0\%$. The magnitude of $\varepsilon_{p,JD}$ increases as the difference in the relative domain fractions increases (i.e. for larger values of $|f - 0.5|$). Figure 14 shows $N_T - 1$ vs. J_{cT} as a function of temperature and domain strain determined by solving eqn (26) for $\alpha = 1$. N_T is always lower than N_i of a single domain for any non-zero domain strain for all f including 0.5 and for $f \neq 0.5$ double valued behaviour of N_T appears. When: $f = 0.5$, N_T is single valued; $f < 0.5$, N_T is higher under tension than compression; $f > 0.5$, N_T is higher under compression than tension. Figure 15 shows $\log(F_{p,\max}[\kappa_1^*]^2)$ versus $\log B_{c2}^*$ as a function of temperature and domain strain with $f = 0.3$ and $\alpha = 1$. For $f \neq 0.5$ double valued behaviour of $F_{p,\max}$ appears as shown in the inset. For: $f = 0.5$ and $\alpha = 1$, $F_{p,\max}$ shows single-valued behaviour with B_{c2}^* comparable to scaling models for homogeneous materials; $f < 0.5$, $F_{p,\max}$ is higher in compression than in tension for the same value of B_{c2}^* ; $f > 0.5$, $F_{p,\max}$ is higher in tension than in compression for the same value of B_{c2}^* .

Eqn (22) shows B_{c2}^* of the system (determined as the lowest field at which $J_{cT} = 0$) is entirely determined by B_{c2i}^* of the domain with the lowest J_{ci} independent of the domain fraction and α (assuming $f \neq 0 \vee 1$ and $\alpha \neq 0 \vee \infty$). For $\alpha = 1$, B_{c2i}^* is the same in each domain when the domain strain is equal and opposite hence, $B_{c2}^*(+\varepsilon_{JD}) = B_{c2}^*(-\varepsilon_{JD})$. However, this is not the case for $J_c(\varepsilon_{JD})$ which is asymmetric for $f \neq 0.5$ and hence, $F_{p,\max}(+\varepsilon_{JD}) \neq F_{p,\max}(-\varepsilon_{JD})$, the result of this is double valued behaviour of $F_{p,\max}$ with B_{c2}^* . The inset in figure 16 shows the relative magnitude of the difference between the tensile and compressive data, $(F_{p,\max}(T, -\varepsilon_{JD}) - F_{p,\max}(T, +\varepsilon_{JD})) / F_{p,\max}(T, +\varepsilon_{JD}) =$

Table 7. Results of fitting eqn (23) to the $\varepsilon_{\text{peak}}$ data for REBCO tape, bronze route [63] and internal tin Nb_3Sn , and jelly roll Nb_3Al wires. $dT_{cA}/d\varepsilon_{\text{JD}}|_{\varepsilon_{\text{JD}}=0\%}$ is coupled with the domain fraction, f , which is calculated using the stated literature values of $dT_{cA}/d\varepsilon_{\text{JD}}|_{\varepsilon_{\text{JD}}=0\%}$. For the LTS materials, it has been assumed that $\alpha = 1$.

	REBCO Tape	Bronze Route Nb_3Sn	Internal Tin Nb_3Sn	Jelly-Roll Nb_3Al
$\varepsilon_{J_{cA}=J_{cB}}$	0.15 ± 0.02	0.31 ± 0.003	0.09 ± 0.006	0.08 ± 0.007
$\frac{f - \alpha(1-f)}{f(1-f)(\alpha+1)^2} \left(\frac{dT_{ci}}{d\varepsilon_{\text{JD}}} _{\varepsilon_{\text{JD}}=0\%} \right)^{-1}$	-0.19 ± 0.02	1.27 ± 0.08	-0.09 ± 0.08	2.0 ± 0.2
f	See Table 6	0.71	0.48	~ 0.5 or 0.67
$dT_{cA}/d\varepsilon_{\text{JD}} _{\varepsilon_{\text{JD}}=0\%}$	Table 6	$0.39 \text{ K}\%^{-1}$ [94]	$0.39 \text{ K}\%^{-1}$ [94]	$0.19 \text{ K}\%^{-1}$
Hysteretic $F_{p,\text{max}} [\kappa_1^*]^2$	Yes $f < 0.5$	Yes $f > 0.5$	No	No

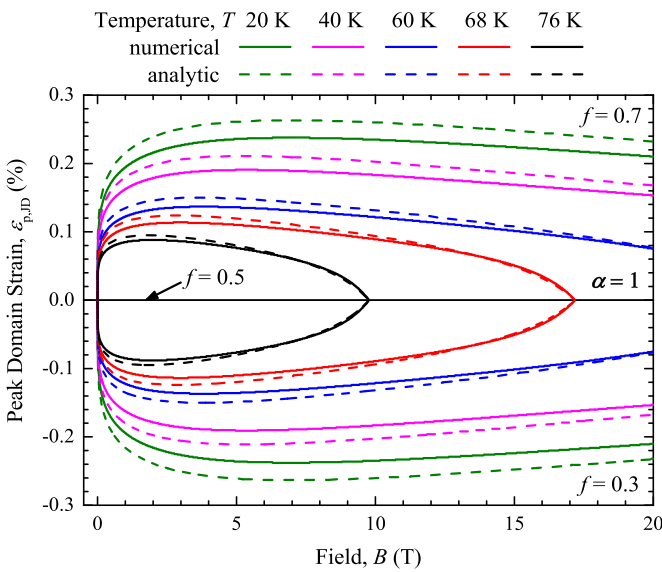


Figure 13. Numerical results for the peak domain strain, $\varepsilon_{p,\text{JD}}$, as a function of field and temperature from the 1D chain model for $f = 0.3$ (bottom half of the panel) 0.5 (horizontal line) and 0.7 (top half of the panel) using the values given in table 5 with $\alpha = 1$. Also shown are the results of the analytically derived equation for $\varepsilon_{p,\text{JD}}$ given by eqn (23) using the same parameters.

$\Delta F_{p,\text{max}}(T, \pm \varepsilon_{\text{JD}})/F_{p,\text{max}}(T, +\varepsilon_{\text{JD}})$, increases and then saturates as the strain increases. We have chosen to characterise this difference at $\varepsilon_{\text{JD}} = \pm 1\%$ because this is large but not unphysical. The model breaks down as $\varepsilon_{\text{JD}} \rightarrow \pm \infty\%$ because one domain is completely suppressed while the other has infinite critical current. Figure 16 shows $\Delta F_{p,\text{max}}(T, \pm \varepsilon_{\text{JD}})/F_{p,\text{max}}(T, +\varepsilon_{\text{JD}})$ as a function of domain fraction at different temperatures for $\varepsilon_{\text{JD}} = \pm 1\%$.

Figure 17 shows how different values of f and α affect the field dependence of $\varepsilon_{p,\text{JD}}$. We find when: $f - \alpha(1-f) = 0$, $\varepsilon_{p,\text{JD}} = 0\%$; $f - \alpha(1-f) < 0$, $\varepsilon_{p,\text{JD}} < 0\%$; $f - \alpha(1-f) > 0$, $\varepsilon_{p,\text{JD}} > 0\%$. J_{cT} is dominated by the domain with the lowest J_{ci} . Conceptually the dependence of $\varepsilon_{p,\text{JD}}$ on α can be understood by recognising that the E -field generated by one domain is not the same as that generated by the other at equal and opposite strain hence, the function is not symmetric and $\varepsilon_{p,\text{JD}} \neq 0\%$. Increasing f or decreasing α for any given strain results in an increase in the ratio of the E -field generated by domain A to domain B. This means a greater tensile strain is required before domain B (which has lower

J_{ci} in tension than domain A) becomes dominant, which results in $\varepsilon_{p,\text{JD}}$ shifting in the tensile direction. The opposite is true when decreasing f or increasing α . The greater the relative difference between J_{cA} and J_{cB} the greater the degree to which J_{cT} is dominated by the weaker domain. The temperature and field dependence of $\varepsilon_{p,\text{JD}}$ is caused by variation of $dJ_{ci}(\varepsilon_{\text{JD}})/d\varepsilon_{\text{JD}}$ with temperature and field. At lower temperatures and fields the magnitude of $dJ_{ci}(\varepsilon_{\text{JD}})/d\varepsilon_{\text{JD}}$ is lower meaning more strain is required to achieve the same relative difference between J_{cA} and J_{cB} . Hence, a lower magnitude of $dJ_{ci}(\varepsilon_{\text{JD}})/d\varepsilon_{\text{JD}}$ means the peak moves to higher compressive or tensile strain (depending on whether $f - \alpha(1-f) < 0$ or $f - \alpha(1-f) > 0$ respectively). The analytical expression for $\varepsilon_{\text{peak}}$, eqn (23), is also compared to the numerical results in figures 13 and 17 showing the expression is a reasonably good approximation with a typical error of $\sim 10\%$.

7. Estimating the domain fraction (f) and the applied strain at which J_c is the same in both domains ($\varepsilon_{\text{app}} = \varepsilon_{J_{cA}=J_{cB}}$) For REBCO,

$\varepsilon_{\text{peak}}$ is plotted against $dT_{cA}/d\varepsilon_{\text{JD}}|_{\varepsilon_{\text{JD}}=0\%} F(N_0, S_N)/g_A(B, T)$ in figure 18 where $dT_{cA}/d\varepsilon_{\text{JD}}|_{\varepsilon_{\text{JD}}=0\%}/g_A$ is given by eqn (25) and we have used all the available data. To calculate $F(N_0, S_N)/g_A(B, T)$, strictly we require the input parameters, $B_{c2}^*(T, \varepsilon_{\text{JD}} = 0\%)$, n , p , q and $T_c^*(\varepsilon_{\text{JD}} = 0\%)$ for an applied strain when $\varepsilon_{\text{JD}} = 0\%$ (i.e. $\varepsilon_{\text{app}} = \varepsilon_{J_{cA}=J_{cB}}$). We initially assume $\varepsilon_{\text{app}} = 0\%$ when $\varepsilon_{\text{JD}} = 0\%$ and calculate the input parameters taken from the detailed flux pinning scaling analysis (cf. Section 5). N_0 values were taken to be their experimental values and w was taken to be the standard value of 2.2. The data at 4.2 K were not included in the analysis due to the systematic inconsistencies in the N -values. Preliminary values of the intercept and gradient ($\varepsilon_{J_{cA}=J_{cB}}$ and $\left(\frac{dT_{cA}^*}{d\varepsilon_{\text{JD}}}|_{\varepsilon_{\text{JD}}=0\%} \right)^{-1} (f(\alpha+1) - \alpha)/f(1-f)(\alpha+1)^2$ respectively) were then extracted from a linear fit to the data. New values of $F(N_0, S_N)/g_A(B, T)$ were calculated with the new value for $\varepsilon_{J_{cA}=J_{cB}}$. After iterating this process, the data in figure 18 were obtained and the final gradient and intercept values obtained are presented in table 7. We note that the data shown in figure 18 are broadly insensitive to the iteration process because the input parameters are predominantly determined by the magnetic field and temperature, and are

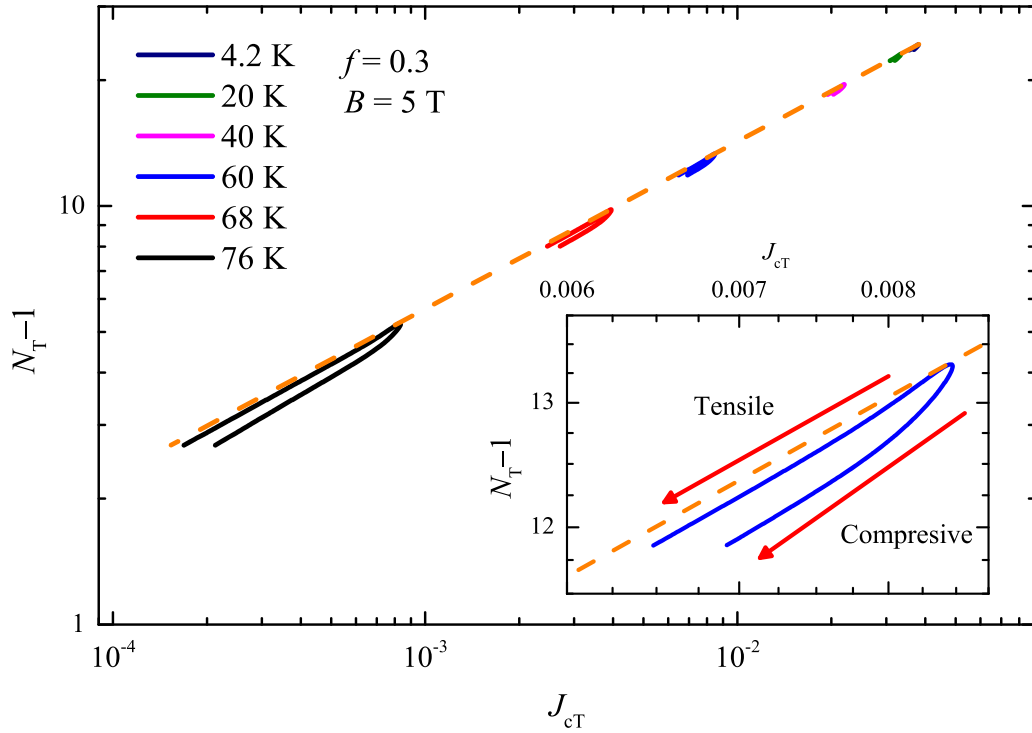


Figure 14. Numerical results for $N_T - 1$ versus J_{cT} in the range $-1\% \leq \epsilon_{JD} \leq +1\%$ at $B = 5$ T when $f = 0.3$ and $\alpha = 1$. The dashed line shows the relation for a single domain. Inset: Detail of data at 60 K.

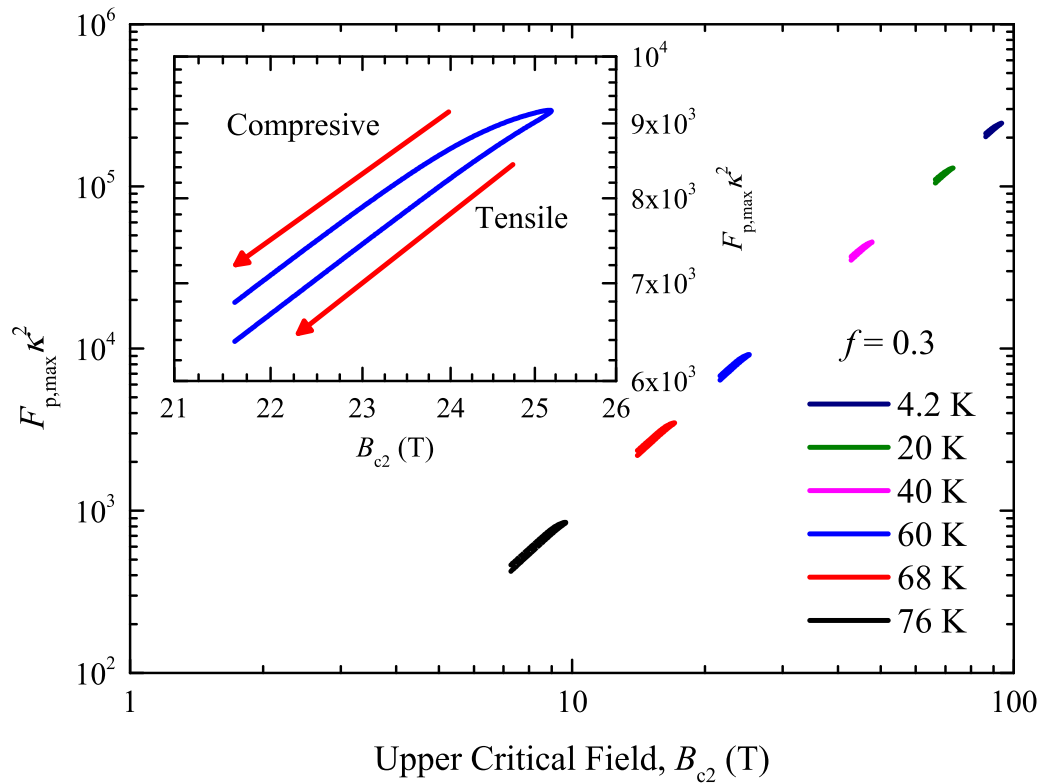


Figure 15. Numerical results for the 1D chain model in the range $-1\% \leq \epsilon_{JD} \leq +1\%$ showing $F_{p,max}$ versus B_{c2}^* on a log-log scale for $f = 0.3$ and $\alpha = 1$. (inset) Detail of the data at 60 K.

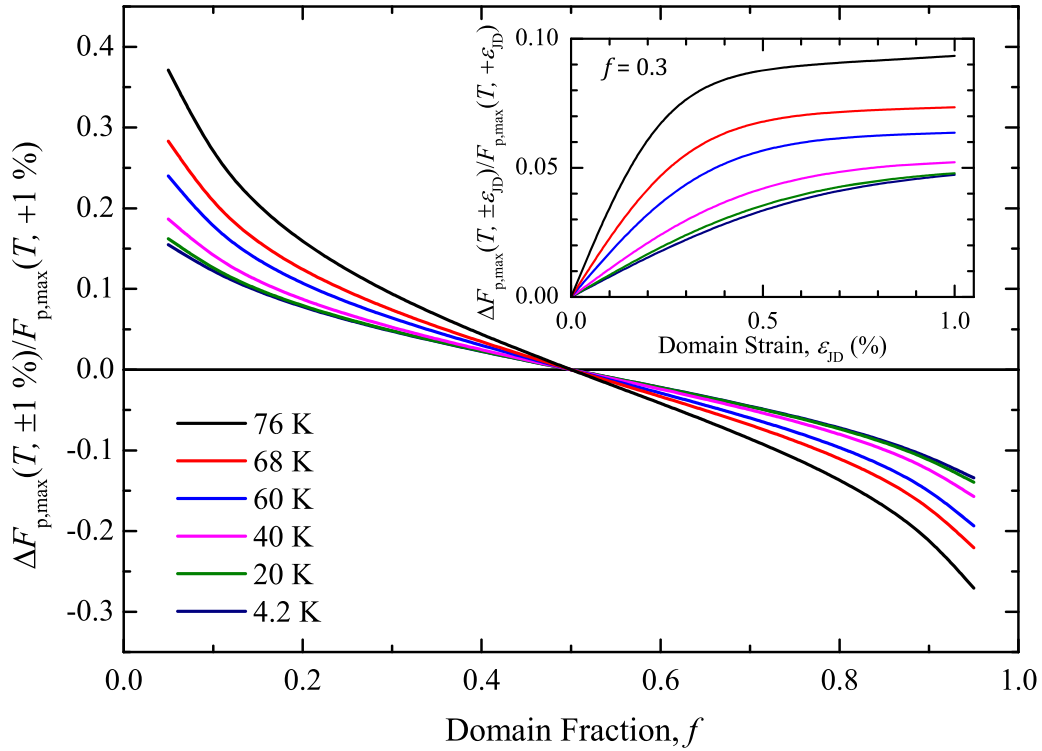


Figure 16. Numerical results for the 1D chain model showing the normalised difference in the double valued behaviour of $F_{p,\max}$ as a function of temperature and f for $\epsilon_{JD} = \pm 1\%$ and $\alpha = 1$, and (inset) as a function of $\pm \epsilon_{JD}$ and temperature for $f = 0.3$ and $\alpha = 1$.

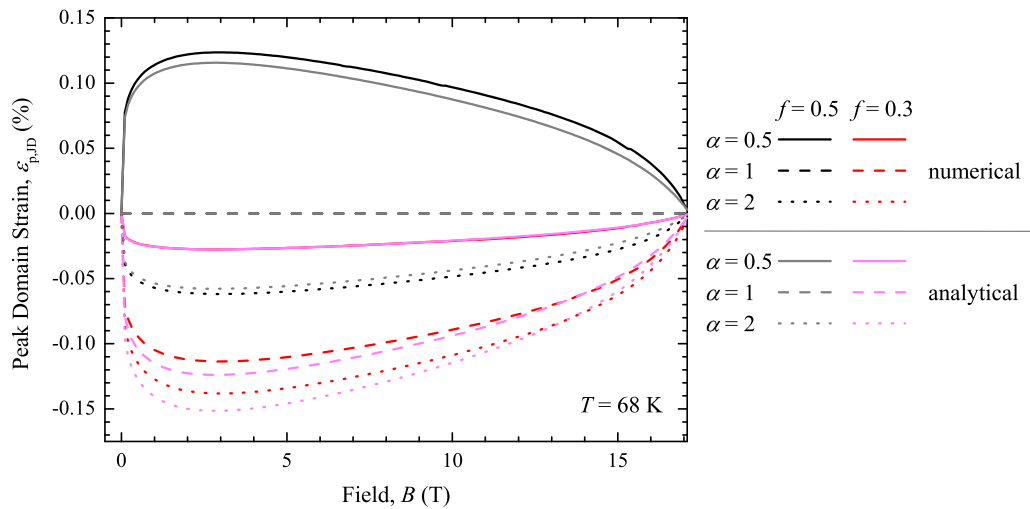


Figure 17. Numerical results for the peak domain strain, $\epsilon_{p,JD}$, at $T = 68$ K as a function of field and α for $f = 0.3$ and 0.5 from the 1D chain model using the values given in table 5. Also shown are the results of an analytically derived equation for $\epsilon_{p,JD}$ given by eqn (23) using the same parameters.

insensitive to small changes in $\epsilon_{J_{cA}=J_{cB}}$. Single crystal values of $dT_{cA}^*/d\epsilon_{JD}|_{\epsilon_{JD}=0\%}$ and α are required to calculate an estimate of f from the gradient. We have used data from the literature for $dT_{cA}^*/d\epsilon_{JD}|_{\epsilon_{JD}=0\%}$ and α listed in table 7 to calculate values of f . We have also measured the relative difference in the double valued behaviour of $F_{p,\max}$ and compared the results to the numerical bimodal chain model results given in figure 16. Given that the compressive data is higher than the

tensile data, we expect $f < 0.5$. Qualitatively we find the same saturation of the normalised difference in $F_{p,\max}$ as a function of strain predicted by the model and from the magnitude of $\Delta F_{p,\max}(T, \pm \epsilon_{JD}) / F_{p,\max}(T, +\epsilon_{JD})$ an estimate of $f \sim 0.42$ for $dT_{cA}^*/d\epsilon_{JD}|_{\epsilon_{JD}=0\%} = 1.6 \text{ K}\%^{-1}$ and $\alpha = 1$ is obtained. The predicted double valued behaviour of N_T is much smaller than the scatter on the experimental N -values and hence was not observed in the experimental data.

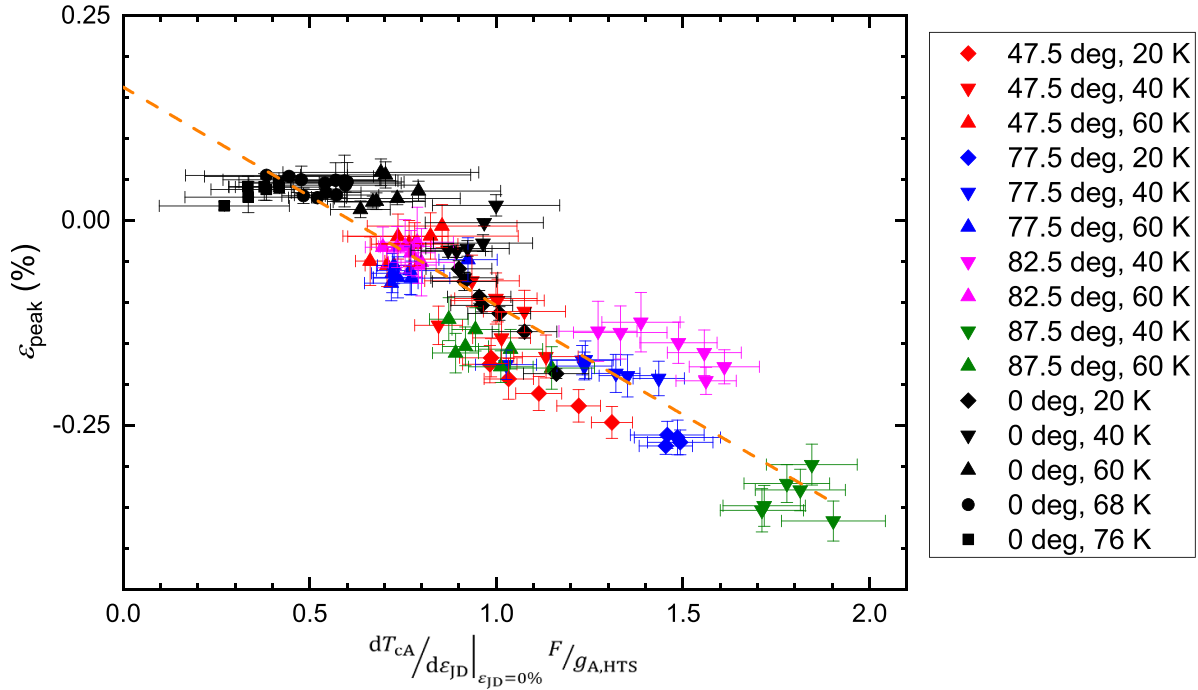


Figure 18. $\varepsilon_{\text{peak}}$ vs. $dT_c/d\varepsilon_{\text{JD}}|_{\varepsilon_{\text{JD}}=0\%} F/g_{\text{A,HTS}}$ including 0 deg data. The uncertainties in $\varepsilon_{\text{peak}}$ are taken directly from the fitting procedure and the uncertainties in $dT_c/de^*(F/g)$ are propagated from the uncertainty in F (the dominant source of uncertainty) [63].

8. The chain model for internal tin Nb_3Sn and Jelly-Roll Nb_3Al

In Durham, we have published detailed critical current density $J_c(B, T, \varepsilon_{\text{app}})$ measurements on many LTS superconducting wires using our 15 T vertical solenoid magnet [18–20, 22, 60, 95, 96]. A variable-temperature Walters’ Spring design [97] has been used to apply strain to the sample. Here we present analytic results derived from the chain model, for previously published internal tin Nb_3Sn , and jelly-roll Nb_3Al wire. The original experimental details of the measurements and the accompanying standard analysis can be found in [60] and [18] respectively. For the LTS materials, the constants found for the parameterisation were obtained without shunt corrections and the functional form of B_{c2}^* was taken to be

$$B_{c2}^*(T, \varepsilon_{\text{app}}) = B_{c2}^*(0, \varepsilon_{\text{app}}) \left(1 - \left(\frac{T}{T_c(\varepsilon_{\text{app}})} \right)^\nu \right) \quad (27)$$

where ν is a free parameter. Equally (cf eqn (25)), we obtain

$$g_{i,\text{LTS}} = \left| \frac{dT_{ci}^*}{d\varepsilon_{\text{JD}}}|_{\varepsilon_{\text{JD}}=0\%} \frac{1}{T_c^*(0)} \left[2 \frac{1+t^2(0)}{1-t^2(0)} + \left(\frac{\nu t(0)}{1-t^\nu(0)} + w \right) \left(\frac{qb(0)}{1-b(0)} + n - p - 2 \right) \right] \right| \quad (28)$$

In contrast to the REBCO tape and the bronze route Nb_3Sn wire reported previously, a single temperature and strain independent value of the exponent n is found to describe the data reasonably well for both the internal tin Nb_3Sn , and the

jelly-roll Nb_3Al wires when the $[\kappa_1^*]^2$ factor is included in the scaling law, and $F_{p,\text{max}}[\kappa_1^*]^2$ is a weakly double-valued or single-valued function of $B_{c2}^*(T, \varepsilon_{\text{app}})$ to within the uncertainties of the experiment. The free parameters obtained are listed in table 2. The chain model analysis was repeated for the two wires as shown in figure 19. The free parameters were taken from the detailed flux pinning scaling analysis (cf. Section 5). The parameter w was taken to be the standard value for a doped LTS material of 2.2 [19]. An estimate of $dT_{cA}^*/d\varepsilon_{\text{JD}}|_{\varepsilon_{\text{JD}}=0\%}$ for Nb_3Sn was obtained from data available in literature. Magnetic measurements on single crystals give $dT_{c100}^*/d\varepsilon_{\text{JD}}|_{\varepsilon_{\text{JD}}=0\%}$ values along the 100 directions that vary by an order of magnitude depending on whether a full screening criterion or an onset criterion was used [94]. We have chosen a value of $dT_{c100}^*/d\varepsilon_{\text{JD}}|_{\varepsilon_{\text{JD}}=0\%}$ of $1.63 \text{ K}\%^{-1}$ characteristic of about 30% screening using a Young’s modulus of 165 GPa [98] to make the stress-strain conversion. This is an upper-bound value along the 100 direction in which the strain dependence is greatest. The random orientation of the grains in Nb_3Sn wires will result in the average value of $dT_{ci}^*/d\varepsilon_{\text{JD}}|_{\varepsilon_{\text{JD}}=0\%}$ being lower. We have taken an approximate average over all solid angles to obtain $dT_{cA}^*/d\varepsilon_{\text{JD}}|_{\varepsilon_{\text{JD}}=0\%} = 0.24 \times dT_{c100}^*/d\varepsilon_{\text{JD}}|_{\varepsilon_{\text{JD}}=0\%} = 0.39 \text{ K}\%^{-1}$ [62]. Single crystal data for Nb_3Al is not available. Since the strain dependence of the critical parameters of Nb_3Al measured in wires is approximately half that of Nb_3Sn for polycrystalline composite wires, we have assumed $dT_{cA}^*/d\varepsilon_{\text{JD}}|_{\varepsilon_{\text{JD}}=0\%} = 0.19 \text{ K}\%^{-1}$. For simplicity, we have assumed a value of $\alpha = 1$. The initial values of $\varepsilon_{J_{cA}=J_{cB}}$ were taken to be 0.14% and 0.12% for the internal tin Nb_3Sn , and jelly-roll Nb_3Al and the values of f and $\varepsilon_{J_{cA}=J_{cB}}$ numbers obtained after iteration are listed in table 7.

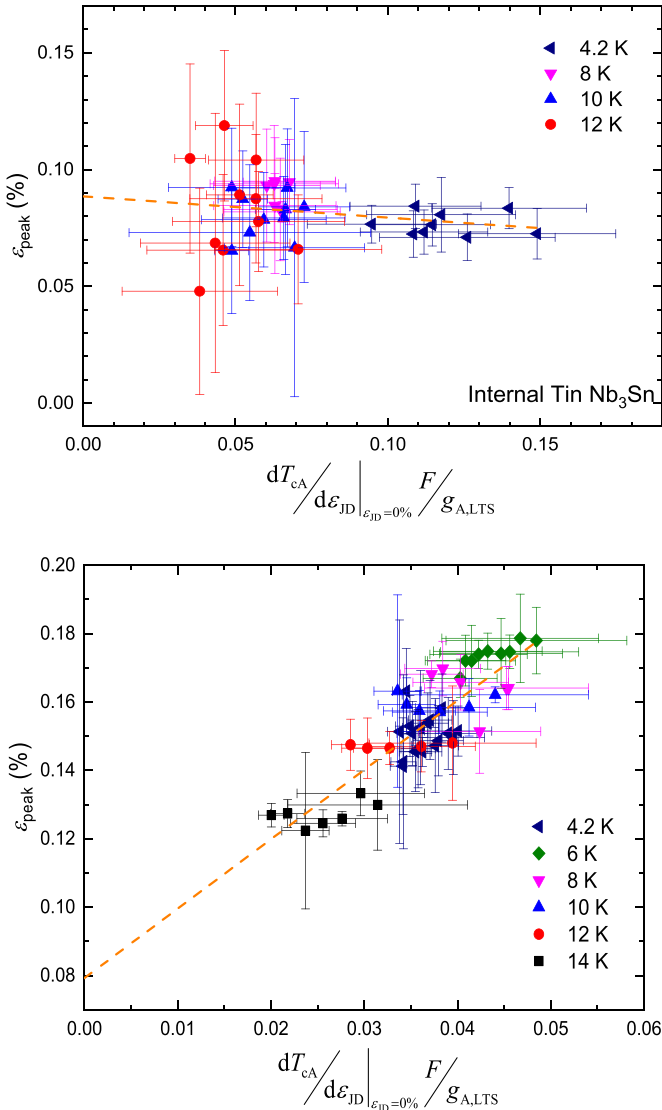


Figure 19. $\varepsilon_{\text{peak}}$ versus $dT_{cA}/d\varepsilon_{JD}|_{\varepsilon_{JD}=0\%} F/g_{A,LTS}$ Top: Internal tin Nb_3Sn wire. Bottom: Jelly-roll Nb_3Al wire. Dashed line is a linear fit to the data with parameters shown in table 7. The parameters $F = N_0/(N_0(N_0 + 1) - 2S_N(N_0 - 1))$ and $g_{A,LTS}$ are given by eqn (28)

In conclusion we find the field and temperature dependence of $\varepsilon_{\text{peak}}$ can be described by the chain model. For the internal tin Nb_3Sn wire $f = 0.5$. The jelly-roll Nb_3Al wire is complex because the peak has a much stronger temperature dependence than field dependence. A least-squares fit to the data as shown in figure 19 gives $\beta = 0.67$.

9. Discussion

For many decades, the magnetic field and temperature dependence of J_c has been measured as part of understanding and increasing J_c for technological applications. More recently, measurements on the strain dependence of J_c have become important because of the large differential strains that occur on cool-down, and the large Lorentz forces that can occur in large scale systems such as CERN [8] or ITER [6]. The

supply of high quality single crystals of REBCO has underpinned extensive data that describe the anisotropic properties of REBCO in-field and under strain including the monotonic and anisotropic strain dependence for T_c for the 2 domains in a 2 G tape. This paper has outlined the chain model in-field and shown that the angular J_c data of 2 G REBCO tapes also shows the marked field and temperature dependence of $\varepsilon_{\text{peak}}$ [35, 52, 53] and so the inverted parabolic strain dependence of J_c (cf Figure 5) can be associated with competing bimodal behaviour and described by the chain model.

9.1. REBCO data

In this paper, we have chosen to investigate a REBCO tape with a simple (i.e. non-APC) microstructure and relatively high J_c . The pinning sites are generally considered to be randomly distributed point defects and the critical parameters are associated with the underlying host matrix of REBCO [56]. We have not considered tapes with higher J_c (for example those that include artificial pinning centres) because such materials with multiple types of pinning site of differing geometries leads to many mechanisms, each with their own field, temperature and strain dependencies that can make it more difficult to deconvolve the underlying science. Even in the non-APC REBCO sample presented here, there is an asymmetry in the angular dependence of J_c at 77 K, 0.5 T associated with additional pinning centres that is not present at 4.2 K, 11 T where the pinning landscape is dominated by the randomly distributed point defects [51].

We have used a combination of phenomenological equations and microscopic equations to characterise J_c and equate the irreversibility field, B_{irr} , found in flux pinning equations, and the upper critical field, B_{c2} , which is a thermodynamic property, to what we have called the effective upper critical field, B_{c2}^* . The irreversibility field is a field below the upper critical field above which $J_c = 0$, despite still being in the superconducting state [99, 100]. The upper critical field delineates the superconducting and normal phases. In figure 20 we compare our resistive transport results for the effective upper critical field to results from literature. RF measurements [101] on a single crystal follow the well-known WHH-like behaviour for B_{c2} found in LTS across the entire temperature range. Magnetic [91, 102] and resistive [103] measurements of B_{c2} on single crystals also show WHH-like behaviour, whereas B_{irr} follows the empirical relation $B_{\text{irr}}(T) = B(0)(1 - T/T_c)^{\beta}$. The resistive measurements performed on the tape sample in this study show behaviour consistent with B_{irr} at both the extrapolated 0% criterion (associated with B_{irr} for single crystals) and the extrapolated 100% criterion (associated with B_{c2} for single crystals). We attribute this behaviour to the architecture of tape samples where the silver, the copper stabilising layers and the sample holder are electrically in parallel with the superconducting layer. When the resistance, caused by dissipation of the superconductor (i.e. in the vortex liquid state), is greater than this parallel resistance the current will shunt through the stabilising metallic layers as well as flowing in the superconducting layer. The voltage is predominantly determined by the current through the shunt. We conclude that the effective upper

critical fields presented in this work are best associated with B_{irr} rather than B_{c2} . A comprehensive analysis would include measurements of B_{c2} and B_{irr} on the same sample. However, this is a formidable challenge, since ideally one would require local probes operating on the scale of the coherence length because these two critical fields vary spatially in high J_c materials, and also a much better understanding than is currently available would be required to extract the characteristic fields for the scaling laws from such measurements.

A temperature dependence for the exponent n is observed in the pinning scaling behaviour of REBCO tape where $f - \alpha(1 - f) \neq 0$ (cf Figure 12) which suggests that the temperature dependence of n may be due to bimodal strain dependence, but is not accounted for by the chain model in its current implementation. Extensions to the model which could account for this behaviour include: distributions of T_{ci}^* in each domain and introducing two or three dimensional percolative current flow. Distributions of T_{ci}^* were implemented in the chain model (data not shown), but this was found to make little difference to the results and did not explain the temperature variation of n . Extending the chain model to two or three dimensions, and introducing percolation and current shunting, may explain the observed behaviour but is beyond the scope of this paper.

A central result in this paper is that the value of $\varepsilon_{\text{peak}}$ varies with field and temperature in our REBCO tape and the chain model can self-consistently describe angular J_c data. The broad features predicted by the chain model can be reproduced as long as there is competition between two components of the material that determine J_c . The simple linear strain dependence of T_c^* in each domain is sufficient to explain both the parabolic behaviour of $J_c(\varepsilon)$ at low strains as well as the non-parabolic behaviour of $J_c(\varepsilon)$ at high strains (i.e. the ‘tails’ at high strains) that have been observed experimentally [46, 48, 51]. In contrast, in a homogeneous model higher order strain dependent terms in T_c^* are arbitrarily added to explain this behaviour. Nevertheless, there are some limitations to the parameterisation we have used to describe the in-field behaviour of J_c . Figure 13 shows that at low fields $\varepsilon_{p,\text{JD}}$ rapidly converges to $\varepsilon_{\text{JD}} = 0\%$ as $B \rightarrow 0\text{T}$. This is a result of the unphysical way in which the flux pinning relation eqn (7) predicts

$$\lim_{B \rightarrow 0\text{T}} J_{ci} = \infty \text{ when } p < 1 \text{ and through eqn (2) } \lim_{B \rightarrow 0\text{T}} N_0 = \infty.$$

A different low-field parameterisation of J_{ci} will result in $\varepsilon_{\text{peak}}$ tending to finite values as $B \rightarrow 0\text{T}$. The chain model also leads to a non-physical discontinuity in the gradient of the strain dependence for the critical parameters T_c^* and B_{c2}^* at $\varepsilon_{J_{cA}} = \varepsilon_{cB}$ because they follow that of the domain with lowest values. This discontinuity is not seen in the data and we expect this discrepancy to diminish if we extend the chain models to 2D or 3D and include the role of percolation and current shunting.

Experimental values of $dT_{ci}^*/d\varepsilon_{\text{JD}}|_{\varepsilon_{\text{JD}}=0\%}$ from the literature for REBCO single crystals [58, 59] and detwinned tapes [93] are summarised in table 7 and used to calculate a range of f values. We attribute the range of $dT_{ci}^*/d\varepsilon_{\text{JD}}|_{\varepsilon_{\text{JD}}=0\%}$ values reported in the literature to differences in the doping and stoichiometry of the samples measured. Although there is no agreement about the value of α or $dT_{ci}^*/d\varepsilon_{\text{JD}}|_{\varepsilon_{\text{JD}}=0\%}$ in the region of $\varepsilon_{\text{JD}} = 0\%$, there is general agreement that

$dT_{ci}^*/d\varepsilon_{\text{JD}}|_{\varepsilon_{\text{JD}}=0\%}$ have opposite signs in the two domains which is the central requirement for the chain model. We have used the high temperature parameterisation of $B_{c2i}^*(T, \varepsilon_{\text{JD}})$ for the analytic derivation of g_{HTS} at high temperatures. At low temperatures, as discussed in section 5, $B_{c2i}^*(T, \varepsilon_{\text{JD}})$ was determined from the flux pinning scaling which gives higher values and a smaller strain dependence as shown in the inset of figure 8. This leads to lower g_{HTS} at low temperatures and higher f . We note this higher value of f is consistent with the magnitude of the double valued behaviour of $F_{p,\text{max}}$.

The temperature dependence of $\varepsilon_{\text{peak}}$ has been reported in literature under self-field conditions [54] and also as a function of field [35, 52, 53]. These results can be described using the bimodal chain model with a value of $f - \alpha(1 - f) < 0$ for references [52–54] and $f - \alpha(1 - f) > 0$ for reference [35]. Osamura *et al* found values of f ranging from 0.36 to 0.65 for a number of lengths of tape assuming $\alpha = 1$ [50]. Analysis of XRD measurements [93] on SuperPower samples with no artificial pinning centres also gives an estimate of the domain fraction to be $f \approx 0.45$. These data show that the values of f in table 7 are reasonable. Inclined Substrate Deposition (ISD) produces tapes with grains aligned 45° from other deposition methods. With this alignment one would expect a homogeneous response of the domains to a uniaxial strain applied along the tape axis. Measurements on ISD [34, 42, 44] and ‘detwinned’ [93, 104] tapes show a linear dependence of T_c^* and J_c to an applied strain indicative of the homogeneous behaviour that is expected in both cases from the chain model. We note that annealing a single tape sample under different stresses in oxygen [93, 104] would lead to a broad range of f values which the chain model predicts would lead to large changes in $\varepsilon_{\text{peak}}$ that could not be explained by the differential thermal contraction used for LTS [105] and suggest that such experiments could usefully enable a stringent test of the chain model.

Stacking faults in the a - b plane are a common feature of high J_c REBCO tapes. It has been shown that the dislocation loops associated with the stacking faults produce a strong additional pinning component when the applied field is increasingly close to being parallel to the a - b plane [87]. At low angles ($\theta \approx 0^\circ$) the flux lines are orthogonal to the dislocation loops and only provide weak pinning. The rigidity of the FLL prevents the fluxons from deforming to follow the dislocation loop, so the interaction volume of the fluxon is not extended along its length. However, at higher angles approaching $\theta = 90^\circ$, where the field is aligned with the a - b planes and the direction of the dislocations, the FLL can distort and it becomes more energetically favourable for fluxons to follow the dislocation loops over an extended portions of their length. This greatly increases the interaction volume and hence, F_p [87]. We have found that the peak in J_c when the direction of the applied field is parallel to a - b plane is more pronounced for higher fields and lower temperatures, consistent with the literature [56, 84, 87]. Literature for samples containing high densities of stacking faults suggests that weak point pinning operates at all fields and temperatures and that the strong pinning provided by stacking faults preferentially operates when

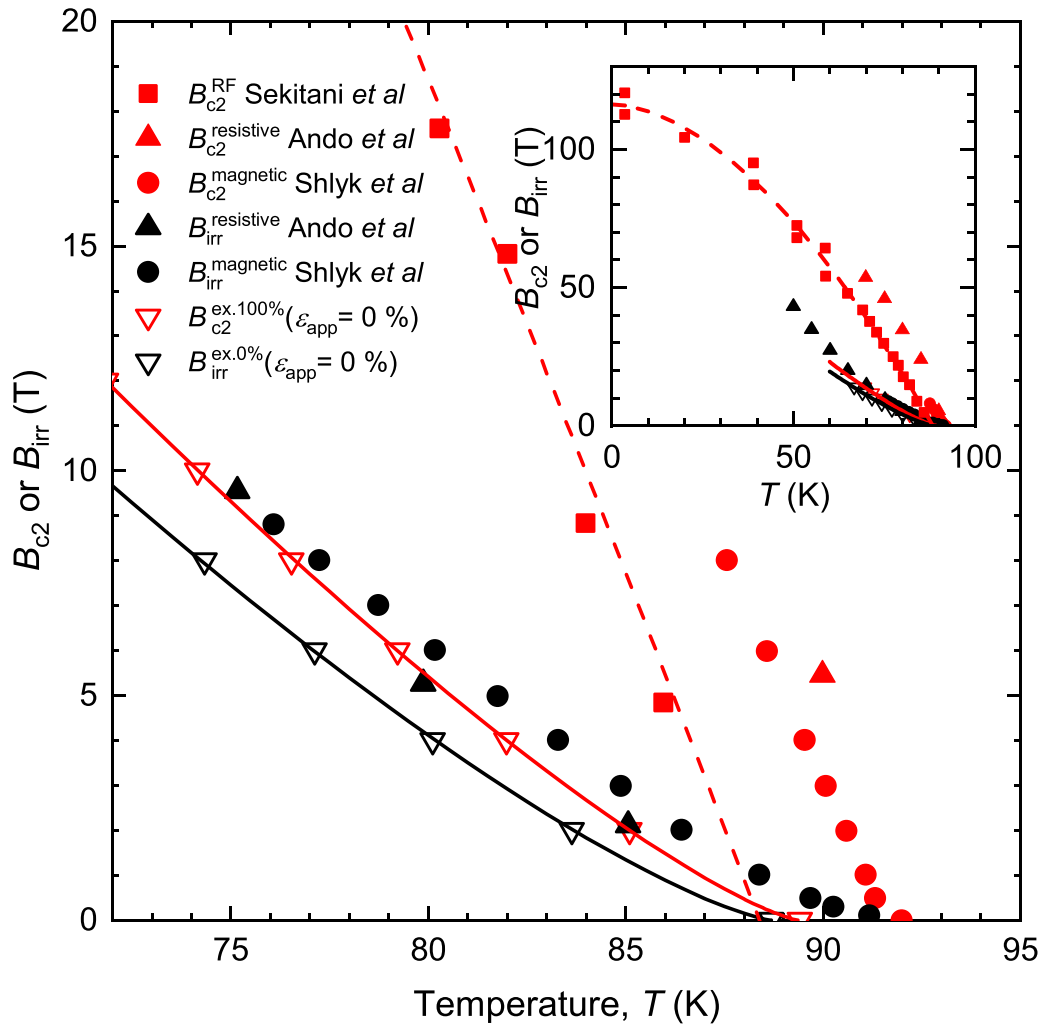


Figure 20. Resistive upper critical field data at $\varepsilon_{\text{app}} = 0\%$ for REBCO tape using the extrapolated 0% and 100% criteria plotted with upper critical field and irreversibility field data from the literature obtained using a variety of techniques on both single crystal and tape samples [91, 101, 103]. Closed symbols are for single crystal and open symbols are for tape. Red and black symbols denote measurement techniques which, for a single crystal, will give B_{c2} and B_{irr} respectively. The solid lines are parameterisations of the extrapolated 0% and 100% data using eqns (3)–(7). The dashed lines are guides for the eye. (inset) Extended temperature range.

$B//a$ - b planes. Associated with the strong angular dependence of J_c when $B//a$ - b planes in high fields and low temperatures, we have found a marked reduction in N (figure 7). This reduction is not consistent with the empirical relation $N = r_N J_c^{S_N} + 1$. The results at $\varepsilon_{\text{app}} = 0.024\%$ and $\varepsilon_{\text{app}} = -0.976\%$ show that strain has little effect on this reduction. We have not found other reports of the reduction of N as a function of angle for high J_c samples. However, a similar drop in N at high angles, despite increases in J_c , has been observed and associated with intrinsic pinning caused by the modulation of the superconducting order parameter in the c -axis direction due to the superconductivity being localised to the CuO_2 planes. Such intrinsic pinning results in a very sharp peak about the ab -plane only a few degrees in width and is not observed in the high J_c samples investigated here, where other sources of pinning dominate over this weak effect and as expected for these high J_c samples that are not perfect single crystals with perfect alignment of the a - b planes between grains. Civale *et al* [85] working on pulsed laser deposition films on

single-crystal SrTiO_3 substrate argue that the reduction in N at low temperatures is caused by thermally activated intrinsic pinning associated staircase behaviour in the FLL when the direction of field is close to the ab -plane [106]. They attribute the weaker suppression of N at higher temperature, independent of field, to the decreasing importance from intrinsic pinning to the overall pinning. We suggest that the arguments Civale *et al* use for intrinsic pinning can be applied to stacking fault pinning to explain the reduction of N observed in this work.

The suppression of N when the direction of the applied field points nearly along the a - b plane has implications for the use of REBCO tapes in magnet windings. Simple pancake windings are often considered optimal for REBCO wound magnets as the maximum deviation of the field angle away from the a - b plane is minimised so higher operational J_c 's can be achieved compared with other winding geometries (such as using Cable On Round Conductor [107]). However, optimal magnet design also requires high values of N to ensure the stability of the

magnet. N is often overlooked in studies of REBCO tapes. This work shows one cannot assume that a high J_c guarantees a high N and that more attention must be paid to the N -values when testing REBCO tapes for use in magnets.

9.2. LTS data

We have not found any substantial experimental evidence for parabolic behaviour of T_c^* under strain for unstrained Nb_3Sn from data on single crystals: In Nb_3Sn , along the 100 direction the strain dependence of T_c is found to be linear with $dT_c^*/d\varepsilon_{100} \approx 1.63 \text{ K}\%^{-1}$. For V_3Si , along 100 direction $dT_c^*/d\varepsilon_{100} \approx +10.6 \text{ K}\%^{-1}$ whereas the opposite behaviour is found along 111 direction where $dT_c^*/d\varepsilon_{111} \approx -0.62 \text{ K}\%^{-1}$ (using a Young's modulus of 233 GPa [108] to make the stress-strain conversion). Hence, we argue that the strain dependence of A15 materials can be considered as multimodal: the critical parameters of some grains increase but with a range of sensitivities to strain that depends on the orientation of each grain to the direction of the applied strain, the critical parameters of other grains decrease again with a different range of strain sensitivities. Without much very detailed single crystal anisotropic strain data on A15 materials, it is not possible to characterise the multimodal behaviour in detail. Nevertheless, even for multimodal materials, the bimodal chain model may still be useful as a proxy model, an approximation where each of the two modes in the model parameterises the averages of those grains with increasing critical parameters and those with decreasing critical parameters. It has long been known that grain boundaries are the dominant pinning mechanism in polycrystalline A15 materials [74, 109, 110]. At J_c , fluxons flow along grain boundary channels with the fluxons in the grains strongly pinned and stationary [80]. Given that the current density in high fields for most polycrystalline materials is typically less than just a few percent of the depairing current density [110, 111], one can consider them as granular to a good approximation. The grain boundaries are complex structures but it is reasonable to assume that they act as barriers that include a central region of low T_c and/or higher resistivity where the superconducting order parameter and the (transport) current density that can cross the grain boundary are severely depressed [112]. In polycrystalline materials, Time Dependent Ginzburg–Landau theory shows that large current densities circulate within and around the edge of the grains [80] with some (transport) current density crossing the grain boundaries. In granular materials, one can expect the transport current density to be percolative, consistent with the relatively small ratio of 2–3 for J_c when measured in longitudinal and transverse orientation of the applied field with respect to the macroscopic current flow in polycrystalline materials [113, 114] and hence, all grain boundaries, both those orthogonal and parallel to the macroscopic current flow direction, contribute to J_c . Given that the critical current through a grain boundary is strongly affected by the thickness of the boundary, we can expect small changes in thickness to produce significant changes in J_c [115]. Consideration of the role of Poisson's ratio leads to competing behaviour from grain boundaries at

different orientations to direction of applied strain. Boundaries orthogonal to an applied tensile strain get wider whereas those parallel to a tensile strain narrow causing J_c to decrease or increase respectively. Hence, applying either tensile or compressive strain always results in J_c across some grain boundaries to decrease and to increase across others. In the context of the chain model and grain boundaries that are highly sensitive to strain, we expect the peak in critical properties to be predominantly associated with the grain boundaries and occur at strains close to the unstrained state in polycrystalline material. These simple considerations also explain the commonly observed experimental asymmetry in the strain dependence of J_c because Poisson's ratio is lower than unity, polycrystalline materials are not completely percolative and the nature of the (non-linear) exponential tunnelling mechanism, all lead to J_c reducing more under tensile strain than an equivalent magnitude of compressive strain. We conclude that polycrystalline superconductors are not best described as homogeneous materials, but as multimodal percolative materials [63]. Whether tension or compression is applied to the material, it consists of competing grains and grain boundary components where some grain boundaries widen and others narrow depending upon their orientation relative to the direction of the applied strain.

To within the accuracy of our data, the $\varepsilon_{\text{peak}}$ data in figure 19 for the internal tin Nb_3Sn conductor shows little or no field and temperature dependence consistent with a value of $f \approx 0.5$ for $\alpha = 1$. A single detailed enough dataset for $\varepsilon_{\text{peak}}$ in an A15 conductor was found in the literature for an internal tin Nb_3Sn conductor and shows similar behaviour [116] (WST sample, data available at [117]). Although double valued behaviour of $F_{p,\text{max}}$ has been observed in literature [118] for two jelly roll internal tin Nb_3Sn wires suggesting $f > 0.5$ for $\alpha = 1$. These results show that as with REBCO the composition and manufacturing process affect the relative fractions, f , of the competing components in Nb_3Sn . The Nb_3Al data appears to show some contradictory behaviour. Figure 19 shows a clear temperature dependence for $\varepsilon_{\text{peak}}$ but only a weak field dependence at each temperature. This is in contrast to the bronze route Nb_3Sn data reported previously [63] where the same value of f is found whether we take variable temperature or variable field data. We note the field dependent behaviour of $\varepsilon_{\text{peak}}$, is only dependent on the accuracy of the universal scaling law (section 5), whereas the temperature dependence is also dependent on our parameterisation of $B_{c2i}^*(0, \varepsilon_{\text{app}})$ with $T_{ci}^*(\varepsilon_{\text{app}})$ through the exponent w . If we allow the possibility that w is anisotropic, it could lead to a temperature dependence of $\varepsilon_{\text{peak}}$ with minimal field dependence for $f \sim 0.5$ and $= 1$. Were we to consider the variable field data alone, we would conclude Nb_3Al is described by the chain model with $f \sim 0.5$ for $\alpha = 1$. If we consider all the field and temperature data we have in figure 19 $f \sim 0.67$ for $\alpha = 1$ as shown in table 7. We note that the changes in $\varepsilon_{\text{peak}}$ for A15 materials as a function of field and temperature are much smaller than those observed in REBCO. This is due to the higher N -values in A15 materials, which act to decrease the magnitude of the changes in $\varepsilon_{p,\text{JD}}$ through eqn (23). Also, differences between $\varepsilon_{\text{peak}}$ and $\varepsilon_{J_{cA}=J_{cB}}$ similar to those observed in this work have been measured using XRD

[119] and these can be better understood in the framework of the chain model.

10. Conclusions

We have performed transport $J_c(B, T, \varepsilon_{\text{app}})$ measurements on samples of REBCO tape over an extensive range of fields ($B \perp$ tape surface for REBCO), temperatures and uniaxial strains. Transport measurements of the effective upper critical field and the critical current density were also performed and engineering parameterisations obtained. Features that cannot be described by standard flux pinning scaling with a homogeneous strain response were observed for REBCO: the parabolic behaviour of $J_c(\varepsilon_{\text{app}})$; the field, temperature and f dependence of the strain at which J_c is a maximum ($\varepsilon_{\text{peak}}$) and the double valued behaviour of $F_{p,\text{max}}$ as a function of B_{c2}^* when the domain fraction is unequal, (i.e. when $f \neq 0.5$).

We have outlined the bimodal chain model to account for the parabolic behaviour of the $J_c(\varepsilon_{\text{app}})$ in REBCO and extended its use to consider the angular dependence of J_c . We find the temperature and field dependence of $\varepsilon_{\text{peak}}$ and double valued behaviour of $F_{p,\text{max}}$ are a natural result of the model. The model is based on two domains with opposing strain dependencies of the critical parameters of relative magnitude α and relative domain fractions of f and $1-f$. We find that the position of $\varepsilon_{\text{peak}}$ is not determined by a peak in the critical parameters but by the combination of the strain responses from the two (monotonic) domains. For $f - \alpha(1-f) < 0$ we find $\varepsilon_{\text{peak}}$ moves further into compression as the temperature or field is lowered and that $F_{p,\text{max}}$ is higher in compression than in tension for the same value of B_{c2}^* . For $f - \alpha(1-f) > 0$ we find $\varepsilon_{\text{peak}}$ moves further into tension and that $F_{p,\text{max}}$ is higher in tension than in compression for the same value of B_{c2}^* . We find $\varepsilon_{\text{peak}}$ is not a function of field and temperature for $f - \alpha(1-f) = 0$, whereas $F_{p,\text{max}}$ is only a single valued function of B_{c2}^* for $f = 0.5$ and $\alpha = 1$. We have also derived an analytic equation for $\varepsilon_{\text{peak}}$ as a function of field, temperature and domain fraction, $\varepsilon_{\text{peak}} = (f - \alpha(1-f))N_0 / \left(gf(1-f)(\alpha+1)^2(N_0(N_0+1) - S_N(N_0-1)) \right) + \varepsilon_{J_{cA}=J_{cB}}$, where the factor g is a function containing the temperature and field dependencies. We suggest weak emergent properties are found in both HTS and LTS high-field superconductors.

Acknowledgments

We would like to thank P. Sunwong and J. Higgins for the development of the strain probe, S. Lishman and A. Davies for help with the design and manufacture of the inverted temperature cup, M. J. Raine for assistance with graphics, and together with A. I. Blair and T. Boutboul at F4E for helpful discussions. We also thank A. Smith for useful discussions about Bc2 and Y. Tsui, N. Cheggour and S. Keys for providing data on Nb₃Sn and Nb₃Al. This work was funded by EPSRC under grant EP/K504178/1. The data in this paper

are available at <http://dx.doi.org/10.15128/gh93gz496> and associated materials are on the Durham Research Online website: <http://dro.dur.ac.uk/>.

ORCID iDs

Kozo Osamura  <https://orcid.org/0000-0002-6401-7237>
Damian Hampshire  <https://orcid.org/0000-0001-8552-8514>

References

- [1] Duyn J H 2012 The future of ultra-high field MRI and fMRI for study of the human brain *Neuroimage* **62** 1241
- [2] Lvovsky Y, Stautner E W and Zhang T 2013 Novel technologies and configurations of superconducting magnets for MRI *Supercond. Sci. Technol.* **26** 093001
- [3] Mitchell N *et al* 2008 The ITER magnet system *IEEE Trans. Appl. Supercond.* **18** 435–40
- [4] Fietz W A, Heller R, Schlachter S I and Goldacker W 2011 Application of high temperature superconductors for fusion *Fusion Eng. Des.* **86** 1365
- [5] Duchateau J L, Komarek P and Turck B 2012 The History of Fusion Magnet Development *100 Years of Superconductivity*, ed H Rogalla and P H Kess (Boca Raton, FL: CRC Press) pp 760
- [6] Sborchia M *et al*, "Overview of ITER Magnet System and European Contribution," *IEEE/NPSS 24th Symp. on Fusion Engineering*, pp.1–8, 2011.
- [7] Weijers H W *et al* 2014 Progress in the Development of a Superconducting 32 T Magnet With REBCO High Field Coils *IEEE Trans. Appl. Supercond.* **24** 4301805
- [8] Rossi L 2010 Superconductivity: its role, its success and its setbacks in the Large Hadron Collider of CERN *Supercond. Sci. Technol.* **23** 034001
- [9] Dimos D, Chaudhari P and Mannhart J 1990 Superconducting transport properties of grain boundaries in YBa₂Cu₃O₇ bicrystals *Phys. Rev. B* **41** 4038–49
- [10] Dimos D, Chaudhari P, Mannhart J and LeGoues F K 1988 Orientation Dependence of Grain-Boundary Critical Currents in YBa₂Cu₃O_{7-d} Bicrystals *Phys. Rev. Lett.* **61** 219–22
- [11] Durrell J H and Rutter N A 2009 Importance of low-angle grain boundaries in YBa₂Cu₃O_{7-δ} coated conductors *Supercond. Sci. Technol.* **22** 013001
- [12] Cheggour N and Hampshire D 1999 Unifying the strain and temperature scaling laws for the pinning force density in superconducting niobium-tin multifilamentary wires *J. Phys. D: Appl. Phys.* **86** 552
- [13] Cheggour N and Hampshire D P 2002 The unified strain and temperature scaling law for the pinning force density of bronze-route Nb₃Sn wires in high magnetic fields *Cryogenics* **42** 299–309
- [14] Ekin J W 1980 Strain scaling law for flux pinning in practical superconductors. Part I: basic relationship and application to Nb₃Sn conductors *Cryogenics* **20** 611–24
- [15] Ekin J W 2010 Unified scaling law for flux pinning in practical superconductors: I. Separability postulate, raw scaling data and parameterization at moderate strains *Supercond. Sci. Technol.* **23** 083001
- [16] Godeke A, Ten Haken B, Ten Kate H H J and Larbalestier D 2006 A general scaling relation for the critical current density in Nb₃Sn *Supercond. Sci. Technol.* **19** R100-R116
- [17] Keys S A and Hampshire D P 2003 A scaling law for the critical current density of weakly and strongly-coupled superconductors, used to parameterise data from a

- technological Nb₃Sn strand *Supercond. Sci. Technol.* **16** 1097–108
- [18] Keys S A, Koizumi N and Hampshire D P 2002 The strain and temperature scaling law for the critical current density of a jelly-roll Nb₃Al strand in high magnetic fields *Supercond. Sci. Technol.* **15** 991–1010
- [19] Taylor D M J and Hampshire D P 2005 The scaling law for the strain dependence of the critical current density in Nb₃Sn superconducting wires *Supercond. Sci. Technol.* **18** S241–S252
- [20] Tsui Y and Hampshire D P 2012 Critical current scaling and the pivot-point in Nb₃Sn strands *Supercond. Sci. Technol.* **25** 054008
- [21] Lu X F and Hampshire D P 2009 The Magnetic Field, Temperature and Strain Dependence of the Critical Current of a Nb₃Sn Strand Using a Six Free-Parameter Scaling Law *IEEE Trans. Appl. Supercond.* **19** 2619–23
- [22] Lu X F and Hampshire D P 2010 The field, temperature and strain dependence of the critical current density of a powder-in-tube (PIT) Nb₃Sn superconducting strand *Supercond. Sci. Technol.* **23** 025002
- [23] Lu X F, Taylor D M J and Hampshire D P 2008 Critical current scaling laws for advanced Nb₃Sn superconducting strands for fusion applications with six free parameters *Supercond. Sci. Technol.* **21** 105016
- [24] Higashikawa K *et al* 2009 Coupled Analysis Method for High-Field Magnet Coil Using Coated Conductor Based on *J-E* Characteristics as a Function of Temperature, Magnetic Field Vector and Mechanical Strain *IEEE Trans. Appl. Supercond.* **19** 1621–5
- [25] Osamura K, Machiya S, Tsuchiya Y and Suzuki H 2010 Force free strain exerted on a YBCO layer at 77 K in surround Cu stabilized YBCO coated conductors *Supercond. Sci. Technol.* **23** 045020
- [26] Osamura K, Sugano M, Machiya S, Adachi H, Ochiai S and Sato M 2009 Internal residual strain and critical current maximum of a surrounded Cu stabilized YBCO coated conductor *Supercond. Sci. Technol.* **22** 065001
- [27] Shin H S, Dedicataria M J, Gorospe A and Lee S H 2015 Experimental measurement of characteristic $I_c(e, q, B)$ response in GdBa₂Cu₃O_d coated conductor tapes under low magnetic field at 77 K *Rev. Sci. Instrum.* **86** 033907
- [28] Cheggour N, Ekin J W, Thieme C L H, Xie -Y-Y, Selvamanickam V and Feenstra R 2005 Reversible axial-strain effect Y-Ba-Cu-O coated conductors *Supercond. Sci. Technol.* **18** S319–S324
- [29] Shin H S *et al* 2015 “Macroscopic Strain Response of I_c Under Magnetic Fields in Differently Stabilized REBCO CC Tapes *IEEE Trans. Appl. Supercond.* **25** 1–4
- [30] Shin H S, Dedicataria M, Gorospe A, Dizon J R, Oguro H and Awaji S, “Strain and Magnetic Field Response of I_c in Reinforced GdBCO Coated Conductor Tapes at 77 K,” *Advances in Cryogenic Engineering, Vol 60*, Proc. Paper vol. 1574, pp. 239–44, 2014.
- [31] Cheggour N *et al* 2003 Reversible axial-strain effect and extended strain limits in Y-Ba-Cu-O coatings on deformation-textured substrates *Appl. Phys. Lett.* **83** 4223–5
- [32] Cheggour N, Ekin J W and Thieme C 2005 Magnetic-Field Dependence of the Reversible Axial-Strain Effect in Y-Ba-Cu-O Coated Conductors *IEEE Trans. Appl. Supercond.* **15** 3577–80
- [33] Sugano M, Osamura K, Prusseit W, Semerad R, Itoh K and Kiyoshi T 2005 strain effect on critical current and its reversibility for YBCO coated conductors with different buffer layers *Supercond. Sci. Technol.* **18** 369–72
- [34] Sugano M *et al* 2005 Reversible strain dependence of critical current in 100 A class coated conductors *IEEE Trans. Appl. Supercond.* **15** 3581–4
- [35] Sugano M, Nakamura T, Manabe T, Shikimachi K, Hirano N and Nagaya S 2008 The intrinsic strain effect on critical current under a magnetic field parallel to the c axis for a MOCVD-YBCO-coated conductor *Supercond. Sci. Technol.* **21** 115019
- [36] Osamura K *et al* 2009 Reversible strain limit of critical currents and universality of intrinsic strain effect for REBCO-coated conductors *Supercond. Sci. Technol.* **22** 025015
- [37] Uglietti D, Seeber B, Abacherli V, Carter W L and Flukiger R 2006 Critical currents versus applied strain for industrial Y-123 coated conductors at various temperatures and magnetic fields up to 19 T *Supercond. Sci. Technol.* **19** 869–72
- [38] Shin H S, Kim K H, Dizon J R, Kim T Y, Ko R K and Oh S S 2005 The strain effect on critical current in YBCO coated conductors with different stabilizing layers *Supercond. Sci. Technol.* **18** S364–S368
- [39] Shin H S, Dedicataria M J and Gorospe A 2016 I_c Strain Performance of REBCO Coated-Conductor Tapes Under Low Magnetic Field *IEEE Trans. Appl. Supercond.* **26** 1–4
- [40] Shin H S, Dedicataria M J, Gorospe A, Oguro H and Awaji S 2016 I_c Response With High Magnetic Field, Low Temperature, and Uniaxial Strain in REBCO Coated Conductor Tapes *IEEE Trans. Appl. Supercond.* **26** 1–4
- [41] Hyung-Seop S, Alking G, Zhierwinjay B and Marlon J D 2016 Evaluation of the electromechanical properties in GdBCO coated conductor tapes under low cyclic loading and bending *Supercond. Sci. Technol.* **29** 014001
- [42] Sugano M, Osamura K, Prusseit W, Semerad R, Itoh K and Kiyoshi T 2005 Tensile fracture behaviour of RE-123 coated conductors induced by discontinuous yielding in Hastelloy C-276 substrate *Supercond. Sci. Technol.* **18** S344
- [43] van der Laan D C, Douglas J F, Goodrich L F, Semerad R and Bauer M 2012 Correlation Between In-Plane Grain Orientation and the Reversible Strain Effect on Flux Pinning in RE-Ba₂Cu₃O_{7-d} Coated Conductors *IEEE Trans. Appl. Supercond.* **22** 8400707
- [44] van der Laan D C *et al* 2011 Anisotropic in-plane reversible strain effect in Y_{0.5}Gd_{0.5}Ba₂Cu₃O_{7-δ} coated conductors *Supercond. Sci. Technol.* **24** 115010
- [45] Zhou C, Yagotintsev K A, Gao P, Haugan T J, van der Laan D C and Nijhuis A 2016 Critical Current of Various REBCO Tapes Under Uniaxial Strain *IEEE Trans. Appl. Supercond.* **26** 1–4
- [46] van der Laan D C, Lu X F and Goodrich L F 2011 Compact GdBa₂Cu₃O_{7-d} coated conductor cables for electric power transmission and magnet applications *Supercond. Sci. Technol.* **24** 042001
- [47] Ilin K *et al* 2015 Experiments and FE modeling of stress-strain state in REBCO tape under tensile, torsional and transverse load *Supercond. Sci. Technol.* **28** 055006
- [48] van der Laan D C 2009 YBCO coated conductor cabling for low ac-loss and high-field magnet applications *Supercond. Sci. Technol.* **22** 065013
- [49] van der Laan D C and Ekin J W 2007 Large intrinsic effect of axial strain on the critical current of high-temperature superconductors for electric power applications *Appl. Phys. Lett.* **90** 052506
- [50] Osamura K, Machiya S and Hampshire D P 2016 Mechanism for the uniaxial strain dependence of the critical current in practical REBCO tapes *Supercond. Sci. Technol.* **29** 065019
- [51] Higgins J S and Hampshire D P 2011 Critical Current Density of YBa₂Cu₃O_{7-d} Coated Conductors Under High Compression in High Fields *IEEE Trans. Appl. Supercond.* **21** 3234–7

- [52] Sunwong P, Higgins J S, Tsui Y, Raine M J and Hampshire D P 2013 The critical current density of grain boundary channels in polycrystalline HTS and LTS superconductors in magnetic fields *Supercond. Sci. Technol.* **26** 095006
- [53] van der Laan D C, Ekin J W, Douglas J F, Clickner C C, Stauffer T C and Goodrich L F 2010 Effect of strain, magnetic field and field angle on the critical current density of $\text{YBa}_2\text{Cu}_3\text{O}_{7-d}$ coated conductors *Supercond. Sci. Technol.* **23** 072001
- [54] Sugano M, Shikimachi K, Hirano N and Nagaya S 2010 The reversible strain effect on critical current over a wide range of temperatures and magnetic fields for YBCO coated conductors *Supercond. Sci. Technol.* **23** 085013
- [55] SuperPower-Furukawa, "High Quality Joints for SuperPower 2G HTS Wire," www.superpower-inc.com/system/files/SP_2G+Wire+Joints_2013FEC_v2.pdf, 2013.
- [56] Yamasaki H, Ohki K, Yamada H, Nakagawa Y and Mawatari Y 2008 Strong flux pinning in $\text{YBa}_2\text{Cu}_3\text{O}_{7-\delta}$ thin films due to nanometer-sized precipitates *Supercond. Sci. Technol.* **21** 125011
- [57] Alok K J *et al* 2015 Tailoring the vortex pinning strength of YBCO thin films by systematic incorporation of hybrid artificial pinning centers *Supercond. Sci. Technol.* **28** 114004
- [58] Fietz W H, Weiss K P and Schlachter S I 2005 Influence of intrinsic strain on T_c and critical current of high- T_c superconductors *Supercond. Sci. Technol.* **18** S332-S337
- [59] Welp U, Grimsditch M, Fleshler S, Nessler W, Downey J and Crabtree G W 1992 Effect of Uniaxial Stress on the Superconducting Transition in $\text{YBa}_2\text{Cu}_3\text{O}_7$ *Phys. Rev. Lett.* **69** 2130
- [60] Lu X F, Pragnell S and Hampshire D P, "Influence of longitudinal strain on the critical current of Nb_3Sn strands," in "ITER Report," Durham University, EFDA/06-1524, 2008.
- [61] Weger M, Silbernagel B G and Greiner E S 1964 Effect of Stress on the Superconducting Transition Temperature of V_3Si *Phys. Rev. Lett.* **13** 521-3
- [62] Pietrass B 1980 Effect of non-hydrostatic stress on the superconducting transition of A15 compounds with high critical temperature *Phys. Status Solidi a* **60** 441-50
- [63] Branch P J, Tsui Y, Osamura K and Hampshire D P 2019 Weakly-Emergent Strain-Dependent Properties of High Field Superconductors *Sci. Rep.* **9** 13998
- [64] Sunwong P, Higgins J S and Hampshire D P 2014 Probes for investigating the effect of magnetic field, field orientation, temperature and strain on the critical current density of anisotropic high-temperature superconducting tapes in a split-pair 15 T horizontal magnet *Rev. Sci. Instrum.* **85** 065111
- [65] Godeke A *et al* 2004 A device to investigate the axial strain dependence of the critical current density in superconductors *Rev. Sci. Instrum.* **75** 5112-8
- [66] van der Laan D C, van Eck H J N, Schwartz J, Ten Haken B and Ten Kate H H J 2002 Interpretation of the critical current in $\text{Bi}_2\text{Sr}_2\text{Ca}_2\text{Cu}_3\text{O}_x$ tape conductors as parallel weak-link and strong-link paths *Physica C* **372-376** 1024-7
- [67] Brandt B L, Liu D W and Rubin L G 1999 Low temperature thermometry in high magnetic fields. VII CernoxTM sensors to 32 T *Rev. Sci. Instrum.* **70** 104-10
- [68] Mei Z, Holder H and Vander Plas H A 1996 Low-Temperature Solders *Hewlett-Packard J.* **10**
- [69] Gurnham C W A, Große V and Hampshire D P, "Angular J_c measurements at 77 K in-field, on an ISD REBCO coated conductor using a straightforward mechanical scribing technique to reduce tape width," *Submitted to EuCAS2019 Glasgow Conf. Proc.*
- [70] Taylor D M J, Keys S A and Hampshire D P 2002 E - J characteristics and n -values of a niobium-tin superconducting wire as a function of magnetic field, temperature and strain *Physica C* **372** 1291-4
- [71] Taylor D M J and Hampshire D P 2005 Relationship between the n -value and critical current in Nb_3Sn superconducting wires exhibiting intrinsic and extrinsic behaviour *Supercond. Sci. Technol.* **18** S297-S302
- [72] Poole C P, Farach H A and Creswick R J 1995 *Superconductivity* (San Diego, California: Academic Press Inc)
- [73] Dew-Hughes D 1974 Flux pinning mechanisms in type II superconductors *Phil. Mag.* **30** 293-305
- [74] Dew-Hughes D 1987 The role of grain boundaries in determining J_c in high-field high-current superconductors *Phil. Mag. B* **55** 459-79
- [75] Kramer E J 1973 Scaling Laws for Flux Pinning in Hard Superconductors *J. Phys. D: Appl. Phys.* **44** 1360-70
- [76] Fietz W and Webb W 1969 Hysteresis in superconducting alloys—Temperature and field dependence of dislocation pinning in niobium alloys *Phys. Rev.* **178** 657-67
- [77] Hampshire D P, Jones H and Mitchell E W J 1985 An in-depth characterisation of $(\text{NbTa})_3\text{Sn}$ filamentary superconductor *IEEE Trans. Magn.* **21** 289-92
- [78] Wilson M N 1986 *Superconducting Magnets* (Oxford : Oxford University Press)
- [79] Tilley D R and Tilley J 1990 *Superfluids: an Introduction Superfluidity and Superconductivity* 3rd edn (Bristol: IOP publishing Ltd) p 18
- [80] Carty G J and Hampshire D P 2008 Visualising the mechanism that determines the critical current density in polycrystalline superconductors using time-dependent Ginzburg-Landau theory *Phys. Rev. B* **77** 172501
- [81] Ekin J W 2007 *Experimental Techniques for Low-Temperature Measurements* (Oxford : Oxford University Press) 464-85 ch. 10
- [82] Hughes I G and Hase T P A 2010 *Measurements and Their Uncertainties: A Practical Guide to Modern Error Analysis* (New York, USA: OUP)
- [83] Uglietti D, Bykovsky N, Sedlak K, Stepanov B, Wesche R and Bruzzone P 2015 Test of 60 kA coated conductor cable prototypes for fusion magnets *Supercond. Sci. Technol.* **28** 124005
- [84] Yamasaki H *et al* 2012 Temperature dependence of magnetic-field angle dependent critical current density and the flux pinning in $\text{YBa}_2\text{Cu}_3\text{O}_7$ thin films *Physica C* **478** 19-28
- [85] Civale L *et al* 2005 Identification of intrinsic ab-plane pinning in $\text{YBa}_2\text{Cu}_3\text{O}_7$ thin films and coated conductors *IEEE Trans. Appl. Supercond.* **15** 2808-11
- [86] Civale L *et al* 2004 Influence of crystalline texture on vortex pinning near the ab-plane in $\text{YBa}_2\text{Cu}_3\text{O}_7$ thin films and coated conductors *Physica C* **412-414** 976-82
- [87] Yamasaki H *et al* 2010 Strong flux pinning due to dislocations associated with stacking faults in $\text{YBa}_2\text{Cu}_3\text{O}_{7-d}$ thin films prepared by fluorine-free metal organic deposition *Supercond. Sci. Technol.* **23** 105004
- [88] Klemm R A, Luther A and Beasley M R 1975 Theory of the upper critical field in layered superconductors *Phys. Rev. B* **12** 877-91
- [89] Smith A P, Raine M J, Surrey E, Awaji S, Okada T and Hampshire D P 2018 3D Properties in (RE)BCO Tapes Measured in Fields up to 35 T. *IEEE Trans. Appl. Supercond.* **29** 6601055
- [90] Tinkham M 1963 Effect of Fluxoid Quantization on Transitions of Superconducting Films *Phys. Rev.* **129** 2413-22
- [91] Shlyk L, Krabbes G, Fuchs G, Nenkov K and Schupp B 2004 Flux pinning and magnetic relaxation in melt-processed

- YBa₂Cu₃O_{7-δ} doped with Li *J. Phys. D: Appl. Phys.* **96** 3371–8
- [92] Machiya S, Osamura K, Shobu T, Kiriya K, Sugano M and Tanaka K 2011 Macroscopic elastic constant analysis and strain behavior of crystal on the YBCO layer in a YBCO-coated conductor *Teion Kogaku* **46** 233–8
- [93] Suzuki T, Awaji S, Oguro H and Watanabe K 2015 Applied Strain Effect on Superconducting Properties for Detwinned (Y, Gd)BCO Coated Conductors *IEEE Trans. Appl. Supercond.* **25** 1–4
- [94] McEvoy J P 1971 Effect of uniaxial stress on the superconducting transition temperature of monocrystalline Nb₃Sn *Physica* **55** 540–4
- [95] Cheggour N and Hampshire D P 1999 Unifying the strain and temperature scaling laws for the pinning force density in superconducting niobium-tin multifilamentary wires *J. Phys. D: Appl. Phys.* **86** 552–5
- [96] Cheggour N and Hampshire D P 2000 A probe for investigating the effect of magnetic field, temperature and strain on transport critical currents in superconducting tapes and wires *Rev. Sci. Instrum.* **71** 4521
- [97] Walters C R, Davidson I M and Tuck G E 1986 Long sample high sensitivity critical current measurements under strain *Cryogenics* **26** 406–12
- [98] Easton D S, Kroeger D M, Specking W and Koch C C 1980 A prediction of the stress state in Nb₃Sn superconducting composites *J. Phys. D: Appl. Phys.* **51** 2748–57
- [99] Farrell D E, Rice J P and Ginsberg D M 1991 Experimental evidence for flux-lattice melting *Phys. Rev. Lett.* **67** 1165–8
- [100] Fisher D S, Fisher M P A and Huse D A 1991 Thermal fluctuations, quenched disorder, phase transitions, and transport in type-II superconductors *Phys. Rev. B* **43** 130–59
- [101] Sekitani T, Miura N, Ikeda S, Matsuda Y H and Shiohara Y 2004 Upper critical field for optimally-doped YBa₂Cu₃O_{7-δ} *Physica B* **346–347** 319–24
- [102] Werthamer N R, Helfand E and Hohenberg P C 1966 Temperature and Purity Dependence of the Superconducting Critical Field, H_{c2} . III. Electron Spin and Spin-Orbit Effects. *Phys. Rev.* **147** 295–302
- [103] Ando Y *et al* 1999 Resistive upper critical fields and irreversibility lines of optimally doped high- T_c cuprates *Phys. Rev. B* **60** 12475–9
- [104] Awaji S, Suzuki T, Oguro H, Watanabe K and Matsumoto K 2015 Strain-controlled critical temperature in REBa₂Cu₃O_y-coated conductors *Sci. Rep.* **5** 11156
- [105] Ochiai S, Osamura K and Watanabe K 1993 Estimation of the strength distribution of Nb₃Sn in multifilamentary composite wire from change in superconducting current due to preloading *J. Phys. D: Appl. Phys.* **74** 440–5
- [106] Blatter G, Feigelman M V, Geshkenbein V B, Larkin A I and Vinokur V M 1994 Vortices in high-temperature superconductors *Rev. Mod. Phys.* **66** 1125–388
- [107] Mulder T, Laan D V D, Weiss J D, Dudarev A, Dhallé M and Kate H H J T 2017 Design and Preparation of Two ReBCO-CORC[®] Cable-In-Conduit Conductors for Fusion and Detector Magnets *IOP Conf. Ser.: Mater. Sci. Eng.* **279** 012033
- [108] Carcia P F and Barsch G R 1973 Elastic properties and superconductivity of V3Si at high pressure *Phys. Status Solidi b* **59** 595–606
- [109] Schauer W and Schelb W 1981 Improvement of Nb₃Sn High Field Critical Current by a Two-stage Reaction *IEEE Trans. Magn.* **17** 374–7
- [110] Wang G, Raine M J and Hampshire D P 2017 How Resistive Must Grain-Boundaries be to Limit J_c in Polycrystalline Superconductors? *Supercond. Sci. Technol.* **30** 104001
- [111] Wang G, Raine M J and Hampshire D P 2017 The Cause of ‘Weak-Link’ Grain Boundary Behaviour in Polycrystalline Bi₂Sr₂CaCu₂O₈ and Bi₂Sr₂Ca₂Cu₃O₁₀ Superconductors *Supercond. Sci. Technol.* **31** 024001
- [112] De Gennes P G 1999 *Superconductivity of Metals and Alloys* (Boulder, Colorado: Perseus Books Group)
- [113] Cullen G W and McEvoy J P 1961 Field and angular dependence of critical currents in Nb₃Sn *Phys. Rev.* **132** 577–80
- [114] Godeke A, Nijhuis A, Ten Haken B and Ten Kate H H J, “Angular dependence of critical current versus magnetic field in Nb₃Sn wires at 9–15 T,” *IOP J Conf. Series*, pp. 917–20, 1997.
- [115] Hsiang T Y and Finnemore D K 1980 Superconducting critical currents for thick, clean superconductor-normal-metal-superconductor junctions *Phys. Rev. B* **22** 154–63
- [116] Ekin J W, Cheggour N, Goodrich L, Splett J, Bordini B and Richter D 2016 Unified Scaling Law for flux pinning in practical superconductors: II. Parameter testing, scaling constants, and the Extrapolative Scaling Expression *Supercond. Sci. Technol.* **29** 123002
- [117] Ekin J W. “ESE Scaling Data.” <http://researchmeasurements.schralpit.com/source-data/>(accessed 13 September 2017).
- [118] Taylor D M J, Keys S A and Hampshire D P 2002 Reversible and irreversible effects of strain on the critical current density of a niobium-tin superconducting wire *Cryogenics* **42** 109–12
- [119] Osamura K *et al* 2012 Local strain and its influence on mechanical–electromagnetic properties of twisted and untwisted ITER Nb 3 Sn strands *Supercond. Sci. Technol.* **25** 054010